Evidence of freezing pressure in sea ice discrete brine inclusions and its impact on aqueous-gaseous equilibrium

O. Crabeck[1,2,†], R. J. Galley[1], L. Mercury [3],B. Delille B[4], J-L. Tison[5] and S. Rysgaard[1,6,7]

[1] Center for Earth Observation Science, Department of Geological Science, University of Manitoba, Winnipeg, MB, R3T 2N2, Canada.
[2] Centre of Ocean and Atmospheric Sciences, School of Environmental Sciences, University of East Anglia, Norwich, NR4 7TJ, United-Kingdom.
[3] Institut des Sciences de la Terre d'Orléans, Centre National de la Recherche Scientifique 45100 Orléans-la-Source, France.
[4] Unité d'Océanographie Chimique, Université de Liège, Liège, 4000, Belgium
[5] Laboratoire de Glaciologie, DGES, Université Libre de Bruxelles, Brussels, 1050, Belgium.
[6] Greenland Climate Research Centre, c/o Greenland Institute of Natural Resources, 3900 Nuuk, Greenland.
[7] Arctic Research Centre, Aarhus University, 8000 Aarhus, Denmark.

[†]Corresponding author: Odile Crabeck (crabecko@myumanitoba.ca / O.Crabeck@uea.ac.uk)

Key Points:

- In discrete brine pockets, our observations show decreased bubble volumes during cooling, and increased bubble volumes during warming.
- Changes of bubble volume are the physical manifestation of changes in the pressure regime within discrete brine inclusions as a function of temperature.
- Freezing pressure builds up in cooled brine inclusions when they evolve as closed systems. This process results in bubble compression.
- These considerations suggest that the use of Henry's Law at constant atmospheric pressure is inadequate to describe the aqueous-gaseous equilibrium in discrete brine inclusions in sea ice.

Abstract

Sea ice in part controls surface water properties and the ocean-atmosphere exchange of greenhouse gases at high latitudes. In sea ice gas exists dissolved in brine and as air bubbles contained in liquid brine inclusions, or as bubbles trapped directly within the ice matrix. Current research on gas dynamics within the ocean-sea ice-atmosphere interface has been based on the premise that brine with dissolved air becomes supersaturated with respect to the atmosphere during ice growth. Based on Henry's Law, gas bubbles within brine should grow when brine reaches saturation during cooling, given that the total partial pressure of atmospheric gases is above the implicit pressure in brine of 1 atm. Using high-resolution light microscopy time series imagery of gas bubble evolution inside discrete brine pockets, we observed bubbles shrinking during cooling events in response to the development of freezing pressure above 3 atm. During warming of discrete brine pockets, existing bubbles expand and new bubbles nucleate in response to depressurization. Pressure variation within these inclusions has direct impacts on aqueous-gaseous equilibrium, indicating that Henry's Law at a constant pressure of 1 atm is inadequate to assess the partitioning between dissolved and gaseous fractions of gas in sea ice. This new evidence of pressure build-up in discrete brine inclusions controlling the solubility of gas and nucleation of bubbles in these inclusions has the potential to affect the transport pathways of air bubbles and dissolved gases within sea ice-ocean-atmosphere interface and modifies brine biochemical properties.

1 Introduction

Sea ice is a multi-phase system formed by the freezing of seawater, which consists of ice, salt precipitates, liquid brine, and air bubbles (WMO, 1970). Gas exists within sea ice in the dissolved state in brine and/or in the gas phase as air bubbles (Cox & Weeks, 1983; Crabeck et al., 2016; Light et al., 2003; Killawee et al., 1998; Tison et al., 2002). Discrete brine pockets are in thermodynamic equilibrium with the ice matrix whose temperature controls the brine volume (V_{Br}) and the chemical concentration of dissolved salts (S_{Br}) and gases in brine (C_{Br}) (Assur, 1960; Cox & Weeks, 1983; Notz & Worster, 2009). Under cooling conditions, brine pockets shrink by freezing water ($H_2O_{(L)}$) out of brine onto the walls of the pocket, until that pockets' increased internal salinity lowers the freezing point of the remaining enclosed brine to the in situ temperature (Assur, 1960) (Fig.1a).

Gas distribution in sea ice depends on: (i) initial gas entrapment at the ice-seawater and ice-atmosphere interfaces; (ii) differential vertical brine (including its dissolved gas) and gas bubble transport within sea ice and across the ice-atmosphere and ice-seawater interfaces, and (iii) potential phase changes in brine pockets via gas exchange between the aqueous (dissolved) and gaseous (bubble) phases in order to maintain air-brine equilibrium during temperature changes (Crabeck et al., 2014a; Tsurikov, 1979; Zhou et al., 2013). The aqueous–gaseous phase transition is a function of the gas solubility that describes the amount of dissolved gas in thermodynamic equilibrium with the gas phase at atmospheric pressure (1 atm) as a function of temperature (T) and salinity (S) of the solution. This thermodynamic equilibrium is described by Henry's solubility coefficient ($K_{H(T,S)}$) in mol L^{-1} atm^{-1}) and gives the saturation concentration of gas in a liquid:

$$C_{Br\ Sat} = P \times K_{H(T,S)} \qquad \text{Eq.1}$$

where $C_{Br\ Sat}$ (mol L^{-1}) is the concentration of the gas dissolved in the solution in equilibrium with the pressure (P) of the gas just above the solution (atm). The dependency of K_H on temperature and salinity is described for O_2 in Garcia and Gordon (1992), and for N_2 and Ar in Hamme and Emmerson (2004) in the range of $-2<t<40°C$; $0< S<40‰$. Zhou et al. (2013) showed that these relationships remain valid for the ranges of temperature and salinity found in sea ice. While decreasing temperature increases the solubility coefficient ($K_{H(T,S)}$) promoting the dissolution of gases in brine ("in-gassing"), increasing salinity lowers the solubility coefficient ($K_{H\ (T,S)}$) and causes outgassing of dissolved gases. The net effect of these opposing processes in cooling brines is a net decrease of gas solubility ($K_{H(T,S)}$) due to the strong increase of brine salinity (salinity effect) (Fig. 1b and Fig. 2a). The thermodynamic capacity of a discrete brine pocket for dissolved gases (Fig.1c) can be described as the number of moles of gas ($N_{Br\ sat} = N_{O2\ sat}+N_{N2\ sat}+N_{Ar\ sat}= N_{air\ sat}$) that can be dissolved in a given brine volume (V_{Br}) in L at in situ temperature and brine salinity assuming Henry's equilibrium at 1 atm (P) as in Eq.2:

$$N_{Br\ Sat} = [K_{H(T,S)air} \times P]V_{Br} \qquad \text{Eq.2}$$

According to equation 2, the ability of brine for dissolved gases decreases drastically during cooling because both solubility $K_{H(T,S)}$ and the solvent volume (V_{Br}) decrease with decreasing temperature and act in concert to favor out-gassing (Fig. 1b,c and Fig. 2a). Conversely, the thermodynamic capacity of a discrete brine pocket for dissolved gases (Fig. 1b,c) increases during warming (Eq.2, Fig. 1b,c and Fig. 2b).

While the thermodynamic capacity of brine for dissolved gases decreases during cooling, the actual (observed) gas concentration (C_{Br}) of a closed brine pocket increases with decreasing temperature. Under cooling conditions, brine pockets shrink and as a result their dissolved gas concentration increases (C_{Br}=N_{br}/V_{Br}); this is the so-called brine concentration effect (Fig. 2a). Therefore, during cooling, the increase of dissolved gas concentration (C_{Br}) (Fig. 2a) combined with the out-gassing effect of the decreased thermodynamic capacity of the brine for dissolved gases ($C_{Br\ sat}$) promotes air supersaturation in discrete brine pockets with respect to atmospheric equilibrium (i.e. 1 atm) (Fig. 2a) (Crabeck et al., 2014a, b; Moreau et al., 2014; Tison et al., 2017; Zhou et al., 2013). Conversely, under warming conditions, pure ice ($H_2O_{(s)}$) melts along the walls of discrete brine inclusions, increasing the volume of the pocket and diluting the internal chemical concentration of the brine solution (the dilution effect) (Fig. 2b). While the ability of brine for dissolved gases ($C_{Br\ sat}$) increases during warming, the observed dissolved gas concentration (C_{Br}) in the brine decreases with the input of freshwater from melting pocket walls (Fig. 2b). In this way it has been assumed that discrete brine pockets previously supersaturated during winter cooling evolve toward their respective equilibrium solubility in spring and summer as they warm (Crabeck et al., 2014a, b; Moreau et al., 2014; Tison et al., 2017; Zhou et al., 2013).

In the absence of analytical methods to assess the partitioning of gases between dissolved and gaseous forms in sea ice brine, the saturation state described by equation 3 is commonly used as proxy to estimate the air volume fraction in sea ice (Crabeck et al., 2014a, b, 2016; Moreau et al., 2014; Zhou et al., 2013).

$$\mathrm{Sat} = C_{\mathrm{Br}} / C_{\mathrm{Br\ Sat}} \qquad \text{Eq.3}$$

where $C_{\mathrm{Br},}$ (mol L^{-1}) is the observed gas concentration in brine and $C_{\mathrm{Br\ Sat}}$ (mol L^{-1}) is the expected gas solubility concentration in brine assuming equilibrium with the atmosphere (1 atm pressure). Since brine becomes increasingly supersaturated (i.e. salinity effect and concentration effect) with respect to atmospheric equilibrium as temperatures decrease (Fig. 2a), recent work (Crabeck et al., 2014a, b, 2016; Kotovitch et al., 2016; Moreau et al., 2014; Tison et al., 2002, 2017; Zhou et al., 2013) assumed that the air volume fraction would increase during ice growth because the brine solution would out-gas and bubbles would begin to potentially nucleate and grow within discrete brine pockets. In contrast, they predict decreased air volume fraction as the ice warms during sea ice melt because the ability of brine for dissolved gas increases ("in-gassing effect") due to the dilution effect (Fig. 2b).

However, some evidence to the contrary of these exists in the literature which we draw attention to now and for consideration in future. Light et al. (2003) reported that cooling (-2°C to -25°C) sea ice caused air inclusions to shrink in size, including the disappearance of the smallest bubbles, while warming (-25°C to -2°C) sea ice increased the size of existing air inclusions. Further, Crabeck et al. (2016) showed that the air volume fraction in sea ice does not increase linearly with the saturation state calculated from in situ temperature and salinity at standard pressure conditions, and suggested that bubble nucleation should be limited by the brine pocket size. These studies indicate that the assumption of Henry's Law equilibrium computed for in situ temperature and salinity assuming standard atmospheric pressure in discrete brine pockets in sea ice may not be appropriate. To improve our understanding of the aqueous-gaseous equilibrium within discrete brine pockets, we designed an experiment to obtain high-resolution imagery of bubbles inside brine inclusions under a range of typical in situ temperatures. We present visual evidence of freezing pressure in discrete brine inclusions that indicates Henry's Law at a constant atmospheric pressure of 1 atm is inadequate to assess the partitioning of gas between the dissolved and gaseous fraction in sea ice.

2 Materials and Methods

Ice cores were extracted from land fast sea ice in Young Sound, near Daneborg in NE Greenland in May 2014. The ice was 1.15 m to 1.35 m thick with bottom temperatures near the seawater freezing point decreasing linearly to -4.5°C at the ice surface. Bulk ice salinity profiles were measured in the melt of 10-cm vertical sections using a portable conductivity (S/cm) and temperature (°C) probe (Orion 3 Star, Thermo Scientific) and converting these measurements to practical salinity after Fofonoff and Millard (1983). These profiles were C-shaped with salinity ranging from 7–9 close the ice-atmosphere interface, 3–5 in the interior, and about 10 near the bottom. After extraction, the ice was immediately transported to the Daneborg station where it was stored in chest freezers < -20°C. It was shipped in frozen containers to the University of Manitoba at the end of the field campaign and stored in the dark in a freezer at -30°C. Ex-situ analysis of samples after storage at low temperatures is an established protocol since there is no method that preserves the in situ sea ice temperature gradient after extraction.

Columnar sea ice samples analyzed here were taken from the inner part of each core from a depth of 70–80 cm to avoid bias due to potential brine movement during sampling or storage. These samples displayed enclosed and isolated brine inclusions with typical morphology upon retrieval from storage. Small subsamples of 5 × 5 × 5 mm were placed in a cooling stage (Linkam THMS600, accuracy ±0.1°C for temperatures between -100°C and +25°C) attached to a Leica DM2500 light microscope. Brine inclusions containing air bubbles were then observed over a -1°C to - 22°C temperature range in transmitted light using 5×, 10×, 20× and 50× magnification. We limited the temperature range to >-22°C to avoid salt precipitation in inclusions (the eutectic point of hydrohalite is -21.79°C, Assur (1960)). Photos were recorded with a Leica DFC295 digital camera, which produced 2048 × 1536 pixel images with a pixel size of 1.2 × 1.2 µm (5× magnification), 0.6 × 0.6 µm (10×), 0.3 × 0.3 µm (20×) and 0.12 x 0.12 µm (50× magnification). The observed change of brine volume with temperature followed the one predicted by the freezing equilibrium relationship (Cox & Weeks, 1983) (r^2=0.92, P>0.01), so we conclude that these experiments were carried out at thermodynamic equilibrium. Image analyses conducted to quantitatively measure morphometric characteristics of air bubbles and brine inclusions were performed using ImageJ software.

Since the circularity (minor diameter/major diameter) of the bubbles observed was above 0.8, we assumed that air bubbles were fully spherical, computing their volume using $V_{Bu} = 4/3\pi r^3$. Discrete brine inclusions are typically elongated in the vertical direction, generally tubular in shape (Light et al., 2003; Golden et al., 2007; Perovich and Gow, 1996; Weissenberger et al., 1992). We therefore approximated them with cylindrical ellipsoids and computed their cylindrical volume ($V_{Br} = \pi H r^2$) where H is the length of the inclusion (major diameter) and r the radius (½ × minor diameter) of the inclusion. The image derived brine volume was compared to brine volume calculated using the equations of Cox and Weeks (1983) with the experimental temperature and bulk ice salinity from the cores at each temperature considered. The salinity dependent equation for the freezing point of seawater at 1 atm total pressure in Notz and Worster (2009) was used here to estimate brine salinity (S_{Br}) from the experimental temperature assuming ice-brine equilibrium.

3 Results

3.1 Cooling experiments

Morphological changes to discrete brine inclusions were observed as they were cooled from -0.8°C to -21°C (Fig. 3a-c), -5°C to -11°C (Fig. 4a-c) and from -15°C to -21°C (Fig. 5a-b) (Table 1). During cooling sequences, the bubble and brine volumes decreased simultaneously suggesting that the change of bubble volume is temperature dependent as is the change in brine volume (Fig. 3b, Fig. 4b). During the cooling sequence shown in Fig. 3a (experiment 1), the bubble volume was reduced by more than 98%, and the volume of the brine inclusion was reduced by 96% (Fig. 3b). The change of bubble volume followed exactly the change in brine volume (1:1 relationship) until -15°C where we observed deviation from the 1:1 relationship (Fig. 3c). During the cooling sequence shown in Fig. 4a (experiment 2), the evolution of bubble and brine volumes were highly correlated, though the change of bubble volume deviated from the 1:1 relationship below -9°C and displayed a higher slope than the 1:1 slope (Fig. 4c). The brine volume was slowly reduced by 62% (Fig. 4b) while the bubble shrunk abruptly in size until it disappeared at -11°C (Fig. 4a). Similarly, during the cooling sequence shown in Fig. 5 (experiments 3 and 4), we observed the reduction in size of two bubbles until they fully collapsed at -20°C and -21°C, respectively. These deviations from the 1:1 relationship between brine and bubble volume suggest the occurrence of processes acting solely on the bubble volume. These processes are powerful enough to homogenize the liquid-air assemblage within discrete brine pockets into a liquid-only phase. Since the two brine inclusions from experiment 3 and 4 (Fig. 5a) are irregularly shaped, we did not derive the brine volume from the image. Instead we computed the expected change of brine volume using the equations from Cox and Weeks (1983) (Fig. 5b).

3.2 Warming experiments

During each warming experiment from -21°C to -7°C (Fig. 6a-c, experiment 5), -4°C to -1°C (Fig. 7a-c, experiment 6) and from -21°C to -5°C (Fig. 8a-e, experiments 7-8) both the bubbles and brine inclusions expanded simultaneously. For experiment 5, the change in bubble volume with temperature (Table 1, Fig. 6a-c) was slightly weaker than the change in brine volume (Fig. 6c) and deviated from the 1:1 relationship. The deviation is maximal in the middle of the temperature range (Fig. 6c). In experiment 6 (Table 1, Fig. 7a-c) below -2.5°C, the change in bubble volume followed the change in brine volume in response to temperature (Fig. 7c) while above -2.5°C the bubble volume change was smaller than the change in brine volume, deviating from 1:1 relationship (Fig. 7c). Finally, in the warming experiments 7 and 8 in Table 1 (-21°C to -5°C, Fig. 8a-e) two bubbles nucleated within discrete brine pockets close to -5°C (Fig. 8b is a time series subset at -5°C of the rightmost two images in Fig. 8a). Experiments 7 and 8 started with a homogeneous brine liquid devoid of bubbles at -21°C, we observed brine expansion without any nucleation until -5°C (Fig. 8a). At -5°C, the upper bubble nucleated first at 0.5s after the last image of brine with no bubble and the lower bubble nucleated after 3.7s (Fig. 8b). Once formed, the bubble volume increased rapidly until it reached a plateau of constant volume. The upper bubble grew by 230% between t=0.5s and t=4.8s (ΔV_{Br} = 122% in the same time-lapse), and the lower one by 214% between t=3.7s and t= 4.8s (ΔV_{Br} = 136% in the same time-lapse).

4 Discussion

In order to simulate gas distribution within sea ice, and extend those simulations to gas flux estimates between the ocean and the atmosphere in the presence of sea ice, previous studies (Crabeck et al., 2014a, b, 2016; Moreau et al., 2014; Tison et al., 2002, 2017; Zhou et al., 2013) applied Henry's Law to aqueous-gaseous equilibrium in brine inclusions, assuming standard atmospheric pressure. These studies predicted that the amount of gas residing in bubbles should increase during cooling as the thermodynamic capacity of brine for dissolved gases decreases (Fig. 1 and 2).

Our results show that despite predicted out-gassing behavior during cooling events, air bubble volumes decreased, and bubbles were in some cases driven back into solution within the liquid brine. During warming events despite the increase thermodynamic capacity of brine for dissolved gases predicting a decrease in air volume fraction (dilution effect, e.g. Fig. 1 and 2), our observations indicate that existing bubbles expanded and new bubbles nucleated. These visual observations suggest that Henry's Law (as in Eq. 1 and 2) at standard pressure conditions (i.e. at 1 atm) should no longer be used to predict the aqueous-gaseous equilibrium in discrete brine pockets in sea ice because (i) it is only valid for a flat infinite interface between the gaseous and aqueous phases and (ii) it implies constant standard atmospheric pressure condition (1 atm) within sea ice brine inclusions. What follows is a discussion of additional processes that should also be accounted for when addressing gas partitioning in sea ice.

4.1 The effect of surface tension

First, the spherical nature of air bubble surfaces in brine inclusions create capillary effects linked to the surface tension (γ, N m^{-1}) of the liquid, unaccounted for by Henry's Law. Surface tension increases the internal pressure of the bubble by an amount equal to the Laplace pressure, which is the pressure difference between the inside and the outside of a curved surface at a gas-liquid interface (Butt et al., 2004):

$$P_{Bu} - P_{sol} = {}^{2\gamma}/_{r} \quad => \quad P_{Bu} = P_{sol} + {}^{2\gamma}/_{r} \qquad \text{Eq. 4}$$

Where P_{sol} is the partial pressure of gas in solution (atm) and P_{Bu} is the partial pressure of gas in the bubble (atm), and r is the radius (m) of the bubble considered as perfectly spherical (Mercury et al., 2003, 2004). Henry's Law therefore needs to be adapted for surface tension effects as:

$$C_{Br\ sat}* = K_{H(T,S)} \times [\mathrm{P_{sol}}+({}^{2\gamma}/_{r})] \qquad \text{Eq. 5}$$

According to Sharqawy et al. (2010), the surface tension of water is a function of temperature and salinity:

$$\gamma_{(T,S)} = 75.59 - 0.13476\,T + 0.021352\,S - 0.00029529\,ST \qquad \text{Eq. 6}$$

Where $\gamma_{(T,S)}$ is the surface tension (mN m^{-1}) of water, T is the temperature in °C ($15 \leq T \leq 35$ °C), S is salinity g Kg^{-1} ($10 \leq S \leq 35$ g kg^{-1}). We extrapolated this relationship to subzero temperatures and to salinity above 35 g kg^{-1}. The surface tension of liquid brine increases by 15% between 0 and -25°C (Fig. 9a). While cooling causes a moderate increase in surface tension of brine (Fig. 9a), it is the much stronger decrease of bubble radius (900% decrease across the observed range of bubble radii, Fig. 9b) that drives the increase of Laplace pressure in Eq. 4. This clearly reduces the impact of the extrapolation of $\gamma_{(T,S)}$ at low temperatures and high salinities in Figure 9a. Based on the Laplace relationship (Eq. 4) the internal pressure of our observed bubbles increased by 0.1 to 1.4 atm with decreasing temperature (Fig. 10a). This pressure increase with decreasing temperature will result in more gas dissolving in the brine but the pressure increase is insufficient to counter balance the decreased solubility due to increased salinity, so overall the amount of gas that can be dissolved in brine still decreases with decreasing temperature (Fig. 10b). Since the system (discrete brine pocket and the bubble therein) is closed, the total number of moles (N_t) of its gas (air = O_2+N_2+Ar) in the system is constant and is composed of the sum of the moles of gas residing in the bubble (N_{Bu}) and in the brine ($N_{Br\,sat}$); ($N_{Br\,sat} + N_{Bu} = N_t$). Since we know the temperature (T), the initial bubble pressure (P_{Bu} considering P_{sol} = 1 atm) using the Laplace relationship (Eq. 4) and the initial volume of the bubble (image derived; V_{Bu} in L), the initial N_{Bu} can be calculated using the Ideal Gas Law (Eq. 7). Henry's Law (Eq. 8) can then be used to calculate the initial number of moles of gas in the brine (N_{Br}):

$$N_{Bu} = \frac{P_{Bu} V_{Bu}}{RT} \qquad \text{Eq. 7}$$

$$N_{Br\,sat} = \left[K_{H(T,S)air} \times P_{Bu}\right] V_{Br} \qquad \text{Eq. 8}$$

Where R = 0.0821 mol atm^{-1} L^{-1} and T is in Kelvin. For a closed brine pocket system in thermodynamic equilibrium with the surrounding ice, Eq. 8 allows us to quantify the effect of decreasing temperature, which increases brine salinity and decreases brine volume, forcing dissolved gas out of solution from the brine (i.e. out-gassing). It also allows tracking of the number of moles of gas dissolved in the brine for different pressure conditions (atmospheric and Laplace-derived relationship) at each experimental temperature. While the increase in pressure due to the Laplace relationship allows for more gas to be dissolved in the brine compared to constant atmospheric pressure conditions (Fig. 10b), the number of moles of gas in the associated bubble should still increase with decreasing temperature due to the degassing of dissolved gases from brine (Fig. 10c) as predicted by past studies (Tison et al., 2002; Zhou et al., 2013; Crabeck et al., 2014a,b; Moreau et al., 2014; Crabeck et al., 2016; Tison et al., 2017). So, although the effect of Laplace pressure should be taken into account when describing the gaseous-aqueous equilibrium in sea ice brine, it cannot explain why bubbles observed here and in Light et al.

(2003) shrink in size and why in some cases they are forced back into the solution during cooling and appear during warming.

4.2 Mechanical compression during cooling

Consider a simple experiment, where a container full with a fixed volume of water is completely frozen, creating an increase in volume of ~10% due to the decrease in density between liquid and solid water. This increase in volume produces pressure on the inside of the container once frozen, and so something has to change to account for that pressure, and often the container will round outwards, increasing to the new required volume. If it does not increase in volume, then the pressure within the container is increased.

Since the change of bubble volume is highly correlated with the change of brine volume, there exists a temperature-dependent process that links the reduction of bubble volume to the reduction of the brine volume. We hypothesize that a decrease in bubble volume due to a decrease in temperature in a closed brine pocket system results from mechanical compression. The freezing pressure associated with the incremental change of $H_2O_{(l)}$ to $H_2O_{(s)}$ from brine as the temperature decrease compresses the contained bubble rather than fracturing the walls of the brine pocket.

According to the Ideal Gas Law, mechanical contraction produces an increase of bubble inner pressure (P in atm) inversely proportional to change of volume (V in L) with decreasing temperature:

$$P_{Bu(T)} = \frac{N_{Bu}RT}{V_{Bu}} \qquad \text{Eq.9}$$

Where R = 0.0821 in atm L mol^{-1} K^{-1} and T is the temperature in Kelvin. As an example in experiment 1 (Table 1 and Fig. 3), the bubble volume was reduced from 20000μm^3 to 300 μm^3 as the temperature decreased from -0.8 to -21°C, which would have increased the pressure within the bubble from 1.1 atm to 67 atm assuming the number of moles of gas in the bubble (N_{Bu}) remained constant (Eq. 9). Because changes in pressure modify the aqueous-gaseous-equilibrium (Eq. 8) in a brine pocket, the number of moles of gas in the brine and in the bubble will be redistributed between the brine and the air bubble until a final, steady-state brine-bubble equilibrium is achieved (Eq. 8 & 9). It is possible to establish the steady state bubble pressure and brine-bubble composition at each temperature with a numerical iteration assuming a closed equilibrium system ($N_{Br\,sat} + N_{Bu} = N_t$) (Table 1. Supp.Mat.). The two constitutive equations are the Ideal Gas Law relating bubble volume and bubble pressure to bubble composition (N_{Bu}) (Eq. 9), and Henry's Law linking the bubble pressure with the composition of the brine at saturation ($N_{Br\,sat}$) (Eq. 8) (Table 1 of Supp. Mat.). The total number of moles in the system is established at the initial temperature of each sequence using Eq. 7 & 8 where P_{Bu} is derived from the Laplace relationship and at each successive temperature $N_{Br\,sat}$ is computed using Eq. 8. First, we applied Eq. 9 to investigate the effect of bubble volume decrease on the bubble pressure. Secondly, because increased pressure in the discrete pocket increases the ability of brine for dissolved gases (Eq. 8), a fraction of the gas residing in the bubble must go into solution in the brine, reducing N_{Bu} for a given volume and temperature. Therefore, to quantify the fraction of gas transferred from the bubble to the brine solution, we recalculated $N_{Br\,sat}$ (Eq. 8) using the pressure from Eq. 9. Since the bubble has lost some of its content to the brine solution, the lowered N_{Bu} promotes a slight decrease of pressure in the bubble in Eq. 9, which in return modifies the ability of brine to hold dissolved gases therefore adjusting $N_{Br\,sat}$ and N_{Bu} for a given volume and temperature. This numerical iteration results in converging P_{Bu}, N_{Bu} and $N_{Br\,sat}$ describing the new steady-state brine-bubble equilibrium for a given volume and temperature of inclusions (Table 1 of Suppl. Mat.). At low temperatures and high pressures, gas behavior tends to deviate from the Ideal Gas Law. For the range of temperatures and pressures observed in this study, the non-ideal gas behavior was estimated with the Van der Waals equation and results showed deviation from ideal gas behavior under 5% on average to a maximum of 10%, so we reasonably assume that gases followed the Ideal Gas Law (Fig.1 of Suppl. Mat) under our experimental conditions.

The results of this numerical iteration are summarized in Fig. 11a-g and are presented for the experiment 1 in Fig. 3d, e and experiment 2 in Fig. 4d, e. Fig. 11e shows that pressure increases with decreasing temperature for experiments 1 and 2 and that this increase of internal gas pressure was sufficiently strong to reverse the decreasing saturation concentration in brine with decreasing temperature (Fig. 11f). At 1 atm the number of moles of dissolved gas decreases drastically with decreasing temperature (Fig. 11g). In this freezing pressure condition, the pressure increase outweighs the out-gassing effects of brine volume decrease (i.e. panel b) and of decreased of $K_{H(T,S)air}$ (i.e. panel d, salinity effect) resulting in a net increase of dissolved gas in brine with decreasing temperature (i.e. panel g). This increase in the thermodynamic capacity of brine for dissolved gases with decreasing temperature under freezing pressure causes the bubble to dissolve and potentially collapse (Fig. 11g). Mass balance calculations also show that although the number of moles of gas is nearly in all cases lower in the brine than in bubbles ($N_{Br\ sat}$:N_t <0.5, Fig. 11g), the range of $N_{Br\ sat}$:N_t values is considerably increased taking into account the pressure build-up effect (freezing pressure) as compared to the atmospheric pressure case (Fig. 11g).

If the change of bubble volume was solely linked to the total pocket volume reduction due to freezing brine, the relative change of bubble volume should follow the relative change of brine volume with temperature, that is the 1:1 relationship in Fig. 3c and Fig. 4c. However, in most experiments the change of bubble volume deviated from the 1:1 relationship (Fig. 3c and Fig. 4c). The additive effect of bulk air transfers from bubble to brine solution as a result of the modified steady-state air distribution between bubble and brine within the inclusion (as described in previous paragraph and in Fig. 11) further impacts the bubble volume. The magnitude of bulk gas transfer between bubble and brine within a discrete pocket depends on the competing effects of (i) increasing pressure promoting gas dissolution (in-gassing) and (ii) out-gassing favored by the concentration effect and salinity effect (i.e. decrease of $K_{H(T,S)air}$) associated to the decrease of brine volume with decreasing temperature (Fig. 11). For example, in experiment 1 illustrated in Fig. 3a, it is only below -15°C that the in-gassing effect linked to the pressure increase (Fig. 3d, e) counterbalanced the out-gassing effect due to salinity effect and decreasing brine volume (Fig. 3e). So, below -15°C, the rising freezing pressure increases the thermodynamic capacity of the brine for dissolved gas overcoming the chemically driven salinity effect and concentration effect, so that the bubble begins to lose moles of gas as they are forced back into the brine solution (Fig. 3e). Similarly, in experiment 2 (Table 1, Fig. 4), the pressure increase in the bubble due to mechanical compression is large enough to overcome the out-gassing effect on the liquid brine caused by increased brine salinity and diminishing brine volume, and the gas is forced back into solution at each observed temperature, eventually causing the bubble to disappear, with its gas content entirely dissolving in the liquid brine (Fig. 4d, e). The mechanical compression due to freezing and the removal of the gas bubble content toward the brine solution by bulk gas transfer act in concert to reduce bubble volume with decreasing temperature and produce substantial deviation from the 1:1 relationship (Fig. 4c).

In summary, our visual observations and calculations indicate that freezing pressure develops in sea ice, in addition to what is expected from surface tension effect when discrete brine pockets are cooled, which causes bubble compression. The bubble volume is reduced (Figs. 3 and 4) because gas is highly compressible while liquid brine is nearly completely incompressible. Secondly, because the thermodynamic capacity of the brine for dissolved gases increases with increasing pressure, bulk transfer of gas from the bubble into liquid brine could occur. This suggests that the increase of internal pressure within a discrete brine pocket driven by cooling must be accounted for in the computation of gas solubility in sea ice brine at a given temperature and salinity.

4.3 Mechanical decompression during warming

When discrete brine pockets are warmed, our observations of bubble nucleation and/or enlargement show that dissolved gases tend to migrate from the dissolved phase in liquid brine to the gas phase in air bubbles (Table 1 and Fig. 6a, c, Fig. 7a, c and Fig. 8a, e), despite the increased solubility of gas in brine with respect to atmospheric pressure as the temperature increases (Fig. 2b: dilution effect and salinity effect). Past studies (Tsurkikov, 1979; Perovich & Gow, 1996; Light et al., 2003) have suggested that the density difference between ice and liquid during melting would result in the formation of so-called "voids". In fact, internal melting upon warming mechanically decompresses discrete brine pockets previously pressurized by cooling allowing gas bubble formation. Applying the same numerical iteration to the imaging results from the warming experiments as we did for the cooling experiments, we computed potential pressure decrease with increasing temperature for experiments 5 and 6 (Table 1, Fig. 6, 7 and 11). In this case, we assumed that at the end of each warming sequence, the final pressure in the brine is 1 atm (P_{sol}=1atm) and the bubble inner pressure is equivalent to that computed with the Laplace relationship (Eq. 4). As for the cooling experiments, the change of bubble volume in response to increasing temperature does not exactly follow the 1:1 relationship with the brine volume (Fig. 6c and Fig. 7c). Decompression allowing mechanical expansion of the bubble also modifies the gaseous-aqueous equilibrium promoting a bulk transfer of gas from the brine to the bubble (out-gassing) as the reduced internal pressure forces gas out of solution. Simultaneously, the increase in brine volume with increasing temperature (dilution effect) promotes the dissolution of gas (in-gassing) (Fig. 1 and Fig 2b). For example, in experiment 6 (Fig. 7), above -2°C, the brine volume increase and its associated salinity decrease act to dissolve gas into the brine (in-gassing), which counterbalances the out-gassing effect of the pressure decrease. The occurrence of gas transfer from the bubble to its surrounding brine reduces the response of bubble volume to the temperature increase (deviation from the 1:1 relationship) (Fig. 7c).

We also observed the nucleation of bubbles upon warming in experiment 7 and 8 (Fig. 8), which started with a homogeneous brine liquid devoid of bubbles. As stated above, the warming should drive gas out of solution as the pressure decreases due to mechanical decompression. The thermal change and the associated melting happen without any nucleation in the liquid phase, meaning the brine becomes supersaturated as the pressure is reduced by the melting. At a certain supersaturation threshold necessary to activate the phase transition, and according to classical nucleation theory, a bubble nucleates and grows rapidly to reach its equilibrium volume (Fig. 8b, d). Similar nucleation processes were observed by Visagie (1969) during the decompression of freezing water droplets. Warming discrete brine inclusions with enclosed bubbles gradually enlarge and therefore gradually decompress, reducing their saturation concentration until they open and connect with the atmosphere and/or ocean, no longer acting as closed systems (Epstein and Plesset, 1950; Vreme et al., 2015).

4.5 Potential inner pressure

Cooling discrete sea ice brine pockets have long been understood to undergo freezing pressure created by volume reduction, which for example is sufficiently high to create cracks and produce brine expulsion (Bennington, 1963; Knight, 1962). In this study, we calculate that the inner pressure of the observed discrete brine inclusions can range from 3 atm to 75 atm (Fig. 11e). We note discrepancy in the ranges of pressure (Exp.1: 1atm $<P_{Bu}<$75 atm; Exp.5: 1atm $<P_{Bu}<$3.5 atm) observed in this work over similar temperature ranges (Exp.1: -21 ºC >T< -1ºC, Exp.5: -21 ºC >T< -7ºC), which we attribute to the importance of the initial conditions of each experiment. The computation of the total number of moles in these closed systems is based on the assumption that for cooling experiments the initial pressure of brine is 1 atm and the pressure inside of the bubble is equivalent to that computed with the Laplace relationship at the beginning of each sequence. While for warming experiments, we assumed that the final pressure of brine is 1 atm and the pressure inside of the bubble is equivalent to that computed with the Laplace relationship at the end of each sequence. In cooling experiment 1 starting at -0.8°C, the pressure condition is probably very close to 1 atm, whereas for cooling experiment 2 or warming experiment 5 starting and finishing at -5 and -7°C, respectively, the pressure conditions are likely greater than 1 atm.

The precise physical-chemical conditions responsible for bubble nucleation as in experiments 7 and 8 or the disappearance of bubbles as in experiments 2 and 4 clearly require further investigation. Studies on freezing pressure based on both experimental observations and theoretical results (King & Fletcher, 1973; Sigunov & Samylova, 2006; Visagie, 1969; Wildeman et al., 2017) demonstrated that the ice shells of frozen water drops are repeatedly able to sustain pressures of tens of atmospheres during freezing. Visagie (1969) and King and Fletcher (1983) reported pressures up to 70 bars (69.08 atm) inside 7 and 10 mm diameter water drops freezing from the outside in. So, if no cracks appear in the inclusions, it is reasonable to expect that when brine inclusions cool and decrease in volume, their internal pressure increases well above 1 atm, affecting the solubility of gas in brine solution, and the variable partitioning of that gas between the dissolved and gaseous phases.

Visagie (1969) and Sigunov and Samylova (2006) studied the effect of enclosed air bubbles on freezing pressure in freezing water drops. They showed that the presence of air bubbles within the freezing water droplet prevented or delayed the development of high pressures in the liquid melt within an ice shell because the pressure increase was taken up by the bubble instead of the liquid due to the difference in compressibility of the two phases. Since water is almost incompressible (compressibility = 5×10^{-10} Pa^{-1}, Fine and Millero, (1973)), only a small part of it has to freeze to result in an internal pressure increase (Wildeman et al., 2017). So it follows that if no bubble existed within the brine, the pressure increase due to freezing would be so strong than the brine pocket would rapidly crack. In the current computation of internal pressure, we assumed that the system was closed and that no crack appears, so that the total amount of salt and gas is constant in the system (brine+bubble), but it is possible that discrete brine pockets depressurize by cracking, which is the postulated mechanism for upward brine expulsion in new growing sea ice (Bennington, 1963; Knight, 1962). For example, Wildeman et al. (2017) observed the formation of cracks on pressurized ice shells and noticed the appearance of vapor cavities on their surfaces (Wildeman et al., 2017). These cracks (Fig. 12a) indicate a sudden change from a high internal pressure to a lower internal pressure (Wildeman et al., 2017). We find evidence of cracks and cavities at the surface of some imaged brine inclusions (e.g. Fig. 12b), and suggest these are evidence of sudden reductions in pressure occurring in discrete sea ice brine pockets. Also, ice spicules are typical indicators of increased pressure inside frozen droplets due to the expansion of the thickening ice shell (Fig 12a, b) (Wildeman et al., 2017), we find visual evidence of spicule-like formations protruding from a discrete brine pocket we imaged during our experiments (Figure 12b).

4.6 Implication for gas exchange

In the schematic model presented in Zhou et al. (2013) and Crabeck et al. (2014a), initial gas incorporation in sea ice preferentially occurs in the dissolved state ($V_a < 1\%$) in the bottom layer. The main transport mechanism in the bottom layer is brine drainage, given that the brine volume is commonly larger than the percolation threshold of 5% (Golden et al., 1998), and that the Rayleigh number (Ra) exceeds the threshold for the onset of convection (critical Rayleigh number (Rac) of 5 or 10 according to Vancoppenolle et al. (2010) and Notz and Worster (2008), respectively). Brine convection (i.e. brine drainage) is the main desalination process in sea ice (Eide & Martin, 1975; Lake & Lewis, 1970; Niedrauer & Martin, 1979; Notz & Worster, 2009; Oertling & Watts, 2004; Untersteiner, 1968; Weeks & Ackley, 1986). Conceivably, brine drainage also causes the loss of dissolved gas (Crabeck et al., 2016; Else et al., 2015; Zhou et al., 2013); its capacity to do so depends on the partitioning of gas between the fraction present in bubbles and that dissolved in brine. Within the warmer sea ice bottom permeable layer, the rejection of dissolved gas into the underlying seawater by brine convection from large and connected brine channels maintains gas concentration close to saturation state. Simultaneously, convective cells trigger the formation of micro bubbles (Crabeck et al., 2016; Zhou et al., 2013), which accumulate near the boundary between the warmer bottom permeable layer and the colder impermeable upper layer of sea ice due to their buoyancy. In the upper impermeable sea ice layer, the brine inclusions begin to disconnect from each other, forming discrete pockets. These enclosed brine inclusions would become supersaturated with respect to air under progressive cooling, assuming that the brine is at constant atmospheric pressure and a portion of the dissolved gas would outgas to gas bubbles (Crabeck et al. 2014a,b, 2016; Zhou et al. 2013).

Our results show that cooling results in increased pressure in closed brine inclusions. Freezing pressure in discrete brine pockets compresses bubbles therein and increases the gas solubility within the brine, meaning that above the bottom permeable layer in sea ice the air volume fraction and the amount of gas trapped in bubbles is reduced. During warming, once discrete liquid brine pockets start to open and connect vertically, depressurization of this brine will force gas out of the solution, promote bubble nucleation, increase the volume of existing bubbles, and buoyancy will still favor rapid degassing to the atmosphere provided that the brine inclusions are sufficiently large and connected (as proposed earlier on in the literature, e.g. Moreau et al. (2014) and Zhou et al. (2013)). Overall, while salt and dissolved gases are mainly rejected downwards in the underlying water, nucleation of gas bubbles and their buoyancy-driven vertical transport remain the main pathways of gas efflux from sea ice to the atmosphere.

Finally, pressure changes may affect the thermodynamic regime of sea ice and other chemical equilibrium reactions than the aqueous-gaseous equilibrium investigated in this study. Preliminary results using FREZCHEM model (V13.3, Marion et al. a 2010) for pressure between 1 and 100 atm showed that build-up pressure does not affect the brine freezing point and the thermodynamic regime of sea ice.

5 Conclusions

Our observations show decreased bubble volumes in discrete brine pockets during cooling, and increased bubble volumes in discrete brine pockets during warming. We have shown that changes of bubble volume are the physical manifestation of changes in the pressure regime within discrete brine inclusions as a function of temperature.

Freezing pressure builds up in cooled brine inclusions when they evolve as closed systems. This process results in bubble compression, lowering bubble volume since air is highly compressible and the liquid brine is not. Secondly, since the solubility of gas in brine increases with increasing pressure, this higher inner pressure allows the liquid brine to hold more dissolved gas than it would at atmospheric pressure. As a result, net bulk diffusion of gas from the bubble into the liquid brine occurs.

Inversely, depressurization during warming enables nucleation processes and forces gas out of solution from the liquid brine. These considerations suggest that the use of Henry's Law at constant atmospheric pressure is inadequate to predict the gas saturation state in discrete brine inclusions. Mass balance calculations show that although the number of moles of gas is nearly always higher in the bubbles, the number of moles of gas in bubbles is considerably reduced taking into account the effect of freezing pressure as compared to the atmospheric pressure case.

We have also shown that surface tension effects due to the bubble shape create a supplementary inner pressure in the bubble, compared to a "flat interface" case. From our observations of relative changes in bubble volume, we however show that this effect is relatively minor compared to the effect of freezing pressure in a closed system.

Prediction of the gas state (dissolved in brine or gaseous in bubbles) in discrete sea ice brine inclusions is important because the vertical transport pathways in sea ice for gas bubbles and dissolved gases are radically different. Dissolved gas in brine tends to be rejected into the underlying ocean by brine drainage. If gases are mainly present in sea ice as bubbles, then the removal of gas from sea ice to the underlying ocean will be moderated by the buoyancy-driven upward migration and accumulation of gas bubbles towards the ice-atmosphere interface. On the other hand, if the gaseous phase in sea ice is reduced or eliminated by freezing pressure, the efficiency of gas exchange with the atmosphere as bubble release during sea ice warming may be affected.

This work demonstrates the occurrence of strong pressure increase in discrete brine inclusions due to mechanical compression during freezing, with further decompression of inclusions during warming. It also demonstrates that this must be taken into account when investigating equilibrium reactions in sea ice, such as gas solubility investigated in this study. The evidence of pressure build-up in enclosed brine inclusions opens new avenues for sea ice research since pressure changes could potentially modify the physical and chemical properties of brine and interactions with air-sea ice-ocean exchanges.

Acknowledgments, Samples, and Data

We gratefully acknowledge the contributions of the Canada Excellence Research Chair (CERC) and Canada Research Chair (CRC) programs. Support was also provided by the Natural Sciences and Engineering Research (NSERC) Council, the Canada Foundation for Innovation and the University of Manitoba. R. J. Galley and S. Rysgaard thank the NSERC discovery grant program. This work is also a contribution to the BIGSOUTH project funded by the Belgian Science Federal Policy Office, and the Fonds de la Recherche Scientique – FNRS (project 2.4517.11). B. Delille is a research associate of the Fonds de la Recherche Scientique – FNRS. This is a MARE contribution. This work is a contribution to the ArcticNet Networks of Centres of Excellence and the Arctic Science Partnership (ASP) asp-net.org. This work has also received the support from the French Agency for Research (ANR) through the Equipex Planex ANR-11-EQPX-36 and the labex Voltaire ANR-10-LABX-100-01. Finally, This work has received funding from the European Union's Horizon 2020 research and innovation program through the EUROCHAMP-2020 Infrastructure Activity under grant agreement No 730997. We would like also thanks Dr. Claudie Hulin for a support and help in the lab and Dr. Vancopenolle for his support with FREZCHEM model. We thank the American Physical Society, and Sander Wildeman and his co-authors for allowing us to reproduce in part a figure of theirs in this work. All the data used within this work are available from the corresponding author or any of the co-authors upon personal communication. We will also endeavor to post these data on the Université de Liège data repository that will provide a permanent link to them.

References

Assur, A. (1960), Composition of sea ice and its tensile strength. SIPRE Research Report 44, U.S. Army snow ice and permafrost research establishment, Corps of Engineers, Wilmette, Illinois, December 1960.

Bennington, K. O. (1963). Some crystal growth features of sea ice. *Journal of Glaciology*, *4*(36), 669-688.

Butt, H. J., Graf, K., & Kappl, M. (2004). Chapter 3: Thermodynamics of interfaces. *Physics and Chemistry of Interfaces* in: *Physics and Chemistry of Interfaces*, 26-41, doi: 10.1002/3527602313.

Cox, G. F. N. & Weeks, C. F. (1983). Equations for determining the gas and brine volumes in sea-ice samples, *Journal of Glaciology*, *29*(102), 306-316.

Crabeck, O., Delille, B., Rysgaard, S., Thomas, D. N., Geilfus, N. X., Else, B., & Tison, J. L. (2014a). First "in situ" determination of gas transport coefficients (, and) from bulk gas concentration measurements (O2, N2, Ar) in natural sea ice. *Journal of Geophysical Research: Oceans*, *119*(10), 6655-6668.

Crabeck, O., Delille, B., Thomas, D., Geilfus, N. X., Rysgaard, S., & Tison, J. L. (2014b). CO2 and CH4 in sea ice from a subarctic fjord under influence of riverine input. *Biogeosciences*, *11*(23), 6525-6538.

Crabeck, O., Galley, R. J., Delille, B., Else, B. G., Geilus, N. X., Lemes, M., ... & Rysgaard, S. (2016). Imaging air volume fraction in sea ice using non-destructive X-ray tomography. *Cryosphere (The)*, *10*, 1125-1145.

Eide, L. I. & Martin, S. (1975). The formation of brine drainage features in young sea ice, *Journal of Glaciology, 14*(70): 137-154.

Else, B. G. T., Rysgaard, S., Attard, K., Campbell, K., Crabeck, O., Galley, R. J., ... & Wang, F. (2015). Under-ice eddy covariance flux measurements of heat, salt, momentum, and dissolved oxygen in an artificial sea ice pool. *Cold Regions Science and Technology*, *119*, 158-169.

Epstein, P. S., & Plesset, M. S. (1950). On the stability of gas bubbles in liquid-gas solutions. *The Journal of Chemical Physics*, *18*(11), 1505-1509.

Fofonof, N. P. and R. C. Millard Jr., (1983), Algorithms for computation of fundamental properties of seawater, UNESCO technical papers in marine science 44,

UNESCO/SCOR/ICES/IAPSO joint panel on oceanographic tables and standards and SCOR working group 51, Paris, France.

Garcia, H. E., & Gordon, L. I. (1992). Oxygen solubility in seawater: Better fitting equations. *Limnology and oceanography*, *37*(6), 1307-1312.

Golden, K. M., Ackley, S. F., & Lytle, V. I. (1998). The percolation phase transition in sea ice. *Science*, *282*(5397), 2238-2241.

Golden, K. M., Eicken, H., Heaton, A. L., Miner, J., Pringle, D. J., & Zhu, J. (2007). Thermal evolution of permeability and microstructure in sea ice. *Geophysical Research Letters*, *34*(16), L16501, doi: 10.1029/2007GL030447.

Hamme, R. C., & Emmerson, S. R. (2004). The solubility of neon, nitrogen and argon in distilled water and seawater. *Deep Sea Research Part I: Oceanographic Research Papers*, *51*(11), 1517-1528.

Fine, R. A., & Millero, F. J. (1973). Compressibility of water as a function of temperature and pressure, *The Journal of Chemical Physics*, *59*(10), 5529-5536.

Killawee, J. A., Fairchild, I. J., Tison, J. L., Janssens, L., & Lorrain, R. (1998). Segregation of solutes and gases in experimental freezing of dilute solutions: Implications for natural glacial systems, *Geochimica et Cosmochimica Acta*, *62*(23-24), 3637-3655.

Kotovitch, M., Moreau, S., Zhou, J., Vancoppenolle, M., Dieckmann, G. S., Evers, K. U., Van der Linden, F., Thomas, D. N., Tison, J.-L., & Delille, B. (2016). Air-ice carbon pathways inferred from a sea ice tank experiment, *Elementa: Science of the Anthropocene,* 4: 00011*2*, doi: 10.12952/journal.elementa.000112.

King, W. D., & Fletcher, N. H. (1973). Pressures and stresses in freezing water drops, *Journal of Physics D: Applied Physics*, *6*(18), 2157.

Knight, C. A. (1962), Polygonization of aged sea ice, *The Journal of Geology*, *70*(2), 240-246.

Lake, R. A. & Lewis, E. L. (1970), Salt rejection by sea ice during growth, *Journal of Geophysical Research, 75*(3): 583-597.

Light, B., Maykut, G. A., & Grenfell, T. C. (2003). Effects of temperature on the microstructure of first-year Arctic sea ice, *Journal of Geophysical Research: Oceans*, *108*(C2), 3051, doi: 10.1029/2001JC000887.

Marion, G., Mironenko, M. & Roberts, M. (2010). FREZCHEM: A geochemical 638 model for cold aqueous solutions, Computers and Geosciences , 36 , 10{15.

Mercury, L., Azaroual, M., Zeyen, H., & Tardy, Y. (2003). Thermodynamic properties of solutions in metastable systems under negative or positive pressures, *Geochimica et Cosmochimica Acta*, *67*(10), 1769-1785.

Mercury, L., Pinti, D. L., & Zeyen, H. (2004). The effect of the negative pressure of capillary water on atmospheric noble gas solubility in ground water and palaeotemperature reconstruction, *Earth and Planetary Science Letters*, *223*(1-2), 147-161.

Moreau, S., Vancoppenolle, M., Zhou, J., Tison, J. L., Delille, B., & Goosse, H. (2014). Modelling argon dynamics in first-year sea ice, *Ocean Modelling*, *73*, 1-18.

Niedrauer, T. M. & Martin, S. (1979). An experimental study of brine drainage and convection in young sea ice, *Journal of Geophysical Research, 84*(C3): 1176-1186, paper number 8C1208.

Notz, D. & Worster, M. G. (2008). In situ measurements of the evolution of young sea ice, *Journal of Geophysical Research: Oceans, 113,* C03001, doi: 10.1029/2007JC0004333.

Notz, D. & Worster, M. G. (2009), Desalination processes of sea ice revisited, *Journal of Geophysical Research: Oceans, 114*, C05006, doi: 10.1029/2008JC004885.

Oertling, A. B., & Watts, R. G. (2004). Growth of and brine drainage from NaCl-H2O freezing: A simulation of young sea ice. *Journal of Geophysical Research: Oceans*, *109*(C4).

Perovich, D. K., & Gow, A. J. (1996). A quantitative description of sea ice inclusions, *Journal of Geophysical Research: Oceans*, *101*(C8), 18327-18343.

Sharqawy, M. H., Lienhard, J. H., & Zubair, S. M. (2010). Thermophysical properties of seawater: a review of existing correlations and data, *Desalination and water Treatment*, *16*(1-3), 354-380, doi: 10.5004/dwt.2010.1079.

Sigunov, Y. A., & Samylova, Y. A. (2006). Pressure growth dynamics during freezing of a closed volume of water with dissolved gases, *Journal of applied mechanics and technical physics*, *47*(6), 842-848.

Tison, J. L., Haas, C., Gowing, M. M., Sleewaegen, S., & Bernard, A. (2002). Tank study of physico-chemical controls on gas content and composition during growth of young sea ice, *Journal of Glaciology*, *48*(161), 177-191.

Tison, J. L., Delille, B., & Papadimitriou, S. (2017). Gases in sea ice, in: *Sea ice*, Thomas, D. N. (Ed.). (2017), John Wiley & Sons, 433-471.

Tsurikov, V. L. (1979). The formation and composition of the gas content of sea ice, *Journal of Glaciology, 22*(86): 67-81.

Untersteiner, N. (1968). Natural desalination and equilibrium salinity profile of perennial sea ice, *Journal of Geophysical Research, 73*(4): 1251-1257.

Vancoppenolle, M., Goosse, H., De Montety, A., Fichefet, T., Tremblay, B., & Tison, J. L. (2010). Modeling brine and nutrient dynamics in Antarctic sea ice: The case of dissolved silica. *Journal of Geophysical Research: Oceans*, *115*(C2).

Visagie, P. J. (1969), Pressures inside freezing water drops, *Journal of Glaciology*, *8*(53), 301-309.

Vreme, A., Pouligny, B., Nadal, F., & Liger-Belair, G. (2015). Does shaking increase the pressure inside a bottle of champagne? *Journal of colloid and interface science*, *439*, 42-53.

Weeks, W. F. & Ackley, S. (1986). The growth, structure and properties of sea ice, in: *The Geophysics of Sea ice*, ed. N. Untersteiner, pages 9-164, Plenum, New York, NY.

Weissenberger, J., Dieckmann, G., Gradinger, R., & Spindler, M. (1992). Sea ice: a cast technique to examine and analyze brine pockets and channel structure, *Limnology and Oceanography*, *37*(1), 179-183.

Wildeman, S., Sterl, S., Sun, C., & Lohse, D. (2017). Fast dynamics of water droplets freezing from the outside in, *Physical review letters*, *118*(8), 084101.

World Meteorological Organization. WMO sea-ice nomenclature. Terminology, codes and illustrated glossary. Edition 1970. Geneva, Secretariat of the World Meteorological Organization, 1970.[ix], 147 p.[including 175 photos]+ corrigenda slip.(WMO/OMM/BMO, No. 259, TP. 145.). *Journal of Glaciology*, *11*(61), 148-149.

Zhou, J., Delille, B., Eicken, H., Vancoppenolle, M., Brabant, F., Carnat, G., ... & Tison, J. L. (2013). Physical and biogeochemical properties in landfast sea ice (Barrow, Alaska): Insights on brine and gas dynamics across seasons. *Journal of Geophysical Research: Oceans*, *118*(6), 3172-3189.

Caption table

Table 1. Change in brine (ΔV_{Br}) and bubble (ΔV_{Bu}) volumes between the initial and final temperatures for each of the individual brine inclusions described in this study, expressed in liter (L) and in % of the initial volume.

Caption figures

Figure 1. (a) Brine volume and brine salinity evolution with decreasing temperatures computed using the state equations of Cox and Week (1983) and brine freezing point equation from Notz and Worster (2009), respectively. (b) Equilibrium concentration in µmol L^{-1} of O_2 ($[O_2]_{sat}$), N_2 ($[N_2]_{sat}$), Ar, ($[Ar]_{sat}$), and air ($[_{Air}]_{sat}$ as the sum of $[O_2]_{sat}$,$[N_2]_{sat}$ and $[Ar]_{sat}$ in brine solution defined by Henry's Law (Eq.1) for atmospheric standard condition ($P_{air}= P_{Ar} + P_{O2} + P_{N2} =1 =0.01+0.21+0.78$ in atm). Solubility coefficient ($K_{H(T,S)}$) in µmol L^{-1} atm^{-1} is computed after Garcia and Gordon (1992) for O_2 and Hamme and Emerson (2004) for N_2 and Ar. (c) The number of moles of gas that can be dissolved in brine solution at Henry's equilibrium for atmospheric standard condition using Eq.2.

Figure 2. Response of physical and chemical parameters involved in the aqueous–gaseous equilibrium to temperature variations in enclosed brine inclusions at constant atmospheric pressure. V_{Br} is the brine volume in L, S is the absolute amount of salt in the inclusion in grams, S_{Br} is the observed brine salinity in g $L^{-1}$of brine. N_{Br} is the absolute number of dissolved moles of gas in the inclusion and C_{Br} is the observed dissolved gas concentration in brine in mol L^{-1} of brine. Since the brine pocket is treated as a closed system S and N_{Br} are constant across temperatures while S_{Br} and C_{Br} vary with the change brine volume (solvent volume in L). $C_{Br\ sat}$

and $N_{Br\ sat}$ are the predicted concentration of dissolved gas (O_2, N_2 and Ar) and absolute number of moles of gas (O_2, N_2 and Ar) at Henry's equilibrium, respectively.

Figure 3. (a) Microphotographs of cooling experiment 1 clearly show decreases in discrete brine pocket size with decreasing temperature and simultaneous decrease in size of a bubble contained therein. (b) Relative volume change ΔV (in %) from initial stage of both the discrete brine pocket and its contained bubble with decreasing temperature computed from the images presented in (a). (c) Relative changes in bubble volume vs. relative changes in brine volume (dotted line is the 1:1 relationship). (d) Bubble inner pressure ($P_{Bu(T)}$) and Henry's constant ($K_{H(T,S)air}$) with decreasing temperature. (e) The number of moles of gas dissolved in brine ($N_{Br\ sat}$:N_t) and in the air bubble (N_{Bu}:N_t) as a fraction of the total number of moles in the closed brine + bubble system with decreasing temperature (see text for details of computation).

Figure 4. (a) Microphotographs of cooling experiment 2 clearly show decreases in discrete brine pocket size with decreasing temperature and simultaneous decrease in size of a bubble contained therein, which eventually disappears. (b) Relative volume change ΔV (in %) from initial stage of both the discrete brine pocket and its contained bubble with decreasing temperature computed from the images presented in (a). (c) Relative changes in bubble volume vs. relative changes in brine volume, (dotted line is the 1:1 relationship, the red line is fitted line using linear regression). (d) Bubble inner pressure ($P_{Bu(T)}$) and Henry's constant ($K_{H(T,S)air}$) with decreasing temperature. (e) The number of moles of gas dissolved in brine ($N_{Br\ sat}$:N_t) and in air bubble (N_{Bu}:N_t) as a fraction of the total number of moles in the closed brine + bubble system with decreasing temperature.

Figure 5. (a) Microphotographs of a cooling experiments 3 and 4 clearly showing decreases in discrete brine pocket size with decreasing temperature and simultaneous decrease in size of a bubble contained therein (upper and lower in each image), which eventually disappear. (b) Relative volume change ΔV (in %) from initial stage of both the discrete brine pocket and its contained bubble with decreasing temperature computed from the images presented in (a) for the bubbles. Because of irregular size of the associated brine inclusions, the theoretical brine volume changes from Cox and Weeks (1983) is shown, instead of the image-measured values.

Figure 6. (a) Microphotographs of warming experiment 5 clearly showing increases in discrete brine pocket size with increasing temperature and simultaneous enlargement of a bubble contained therein. (b) Relative volume change ΔV (in %) from initial stage of both the discrete brine pocket and its contained bubble with increasing temperature computed from the images presented in (a). (c) Relative changes in bubble volume vs. relative changes in brine volume (dotted line is the 1:1 relationship). (d) Bubble inner pressure ($P_{Bu(T)}$) and Henry's constant ($K_{H(T,S)air}$) with increasing temperature. (e) The number of moles of gas dissolved in brine ($N_{Br\ sat}$:N_t) and in air bubble (N_{Bu}:N_t) as a fraction of the total number of moles in the closed brine + bubble system with increasing temperature (see text for details of computation).

Figure 7. (a) Microphotographs of warming experiment 6 clearly showing increases in discrete brine pocket size with increasing temperature and simultaneous enlargement of a bubble contained therein. (b) Relative volume change ΔV (in %) from initial stage of both the discrete brine pocket and its contained bubble with increasing temperature computed from the images

presented in (a). (c) Relative changes in bubble volume vs. relative changes in brine volume, (dotted line is the 1:1 relationship, the red line is fitted using linear regression). (d) Bubble inner pressure ($P_{Bu(T)}$) and Henry's constant ($K_{H(T,S)air}$) with increasing temperature. (e) The number of moles of gas dissolved in brine ($N_{Br\ sat}$:N_t) and in air bubble (N_{Bu}:N_t) as a fraction of the total number of moles in the closed brine + bubble system with increasing temperature.

Figure 8. (a) Selected microphotographs of warming experiments 7 and 8, which show change in the size of brine pockets with increasing temperature from -21°C to -5°C. (b) Selected microphotographs in time series (t = 0.0s to t = 4.8s) at a constant temperature of -5°C following on from the warming shown in (a) showing the nucleation of bubbles in the upper brine pocket at t = 0.5s and in lower brine pocket at t = 3.7s, as well as their enlargement with time. The two last panels of (a) are the first and last panels of (b), as shown by the time signature. (c) Relative volume change ΔV (in %) of the upper and lower discrete brine pockets with increasing temperature computed from the images presented in (a). (d) Relative change of brine and bubble volume as a function of time during the microphotographic time series shown in (b) over 4.8 seconds at a constant temperature of -5°C. (e) Brine volume increase compared with the bubble volume increase during the 4.8 second sequence shown in (b) at -5 °C.

Figure 9. (a) Surface tension of the brine (γ_{Br}, N m^{-1}) extrapolated from Sharqawy et al., (2010) (Eq. 6) as a function of the brine freezing point and brine salinity from Notz and Worster (2009) for the range of temperature and brine salinity observed in this study. (b) The relationship between the bubble radius from experiments 1 to 9 and Laplace pressure for γ = 0.076 N m^{-1} (surface tension of sea water) and γ_{Br} (T,S) after Sharqawy et al., (2010) (Eq. 6). The change of bubble radius controls the development of Laplace pressure while the change of γ_{Br} in (a) with brine salinity and temperature has a negligible effect.

Figure 10. (a) The internal pressure of individual bubbles derived from the Laplace relationship (Eq. 4) using observed bubble radii and $\gamma_{(T,S)}$ (Eq.6) for each of our experiments. (b) The air saturation concentration in brine solution defined by Henry's Law (Eq.1) as $[air]_{sat} = P_{Bu}$ X $K_{H(T,S)air}$ for atmospheric standard condition ($P_{Bu} = P_{Ar} + P_{O2} + P_{N2} = 0.01+0.21+0.78=1=P_{sol}$) and for Laplace relationship ($P_{Bu} = P_{sol} + 2\gamma/r$) in experiment 1. The pressure increase allows for more gas to dissolve in the brine (vertical displacement of the curve in panel (b)), but the amount of dissolved air in brine at equilibrium with the air bubble still decreases with decreasing temperature as a result of the air solubility ($K_{H(T,S)air}$) decreasing with increasing salinity (shape of the curve stay unchanged). (c) The fraction of moles of gas in air bubble (N_{Bu}:N_t) and dissolved in brine ($N_{Br\ sat}$:N_t) in experiment 1 as a function of the temperature for constant atmospheric conditions (open symbols) and considering Laplace pressure relationship (filled symbols). The decrease in $K_{H(T,S)air}$ and V_{Br} with decreasing temperature reduces the ability of brine for dissolved gases and promotes out-gassing at both constant and Laplace pressure.

Figure 11. (a) Temperature ranges for cooling experiments 1 and 2, and warming experiments 5 and 6. (b) Bubble (Bu) and brine (Br) inclusion volumes at cooling and warming intervals shown in (a). (c) Brine salinity (S_{br}) in the four experiments as affected by reduced temperature (i.e. panel a). (d) $K_{H(T,S)air}$, the Henry's Law solubility coefficient for brine. Note the decrease in $K_{H(T,S)air}$ despite decreasing temperature due to the increase of brine salinity (i.e. panel c). (e) The internal bubble pressure computed iteratively, $P_{Bu(T)}$ (i.e. the freezing pressure). (f) The gas saturation concentration in brine at cooling and warming intervals shown in panel (a) computed

using Eq.1 for P = 1 atm (white bars) and for P = $P_{Bu(T)}$ from panel (e) (i.e. plain blue bars = freezing pressure). Using 1 atm, the saturation concentration in brine decreases with decreasing temperature due to the decrease of $K_{H(T,S)air}$ (see panel d). Using increasing freezing pressure ($P_{Bu(T)}$ shown in (e), the saturation concentration increased with decreasing temperature for each of the four experiments. (g) The number of moles of dissolved gas in liquid brine as fraction of the total number of moles in the closed brine + bubble system at cooling and warming intervals at 1 atm pressure (white bars) and under the freezing pressure conditions (blue bars, pressures shown in (e)), $N_{Br\,sat} = (K_{H(T,S)air} \times P_{Bu})V_{Br}$. At 1 atm the number of moles of dissolved gas decreases drastically with decreasing temperature. However, increased freezing pressure overcomes the effect of brine volume decrease (i.e. panel b) and decreased $K_{H(T,S)air}$ (i.e. panel d) resulting in a net increase of dissolved gas in brine with decreasing temperature causing the bubble to lose gas to solution in brine and creates the potential for bubble collapse

Figure 12. (a) Cracks, ice spicules and cavitation on the ice shell of an inward freezing water droplet reproduced from Wildeman et al. (2017). (b) Example of cracks, ice spicules and cavities on surface of a brine inclusion imaged in this paper.

Table:

Exp.	**Sequence**	**Temp (°C)**		**Event**		**V_{Bu} (L)**	**V_{Br} (L)**	**ΔV (%)**	
								ΔV_{Bu}	**ΔV_{Br}**
1	**Cooling**	T_i	-0.8		V_i	$2.1\ 10^{-11}$	$4.5\ 10^{-10}$	-98	-96
		T_f	-21		V_f	$2.9\ 10^{-13}$	$2.1\ 10^{-11}$		
2	**Cooling**	T_i	-5	Bubble collapses at -10	V_i	$3.7\ 10^{-11}$	$5.9\ 10^{-10}$	-100	-60
		T_f	-11		V_f	0	$2.4\ 10^{-10}$		
3	**Cooling**	T_i	-15	Bubble collapses at -21	V_i	$2.7\ 10^{-12}$	Na	-100	Na
		T_f	-21		V_f	0	Na		
4	**Cooling**	T_i	-15	Bubble collapses at -21	V_i	$2.7\ 10^{-11}$	Na	-100	Na
		T_f	-21		V_f	0	Na		
5	**Warming**	T_i	-21		V_i	$4.7\ 10^{-12}$	$5.7\ 10^{-11}$	273	315
		T_f	-7		V_f	$1.3\ 10^{-11}$	$1.8\ 10^{-10}$		
6	**Warming**	T_i	-4		V_i	$1.8\ 10^{-12}$	$1.1\ 10^{-10}$	431	225
		T_f	-1		V_f	$7.8\ 10^{-12}$	$2.4\ 10^{-10}$		
7	**Warming**	T_i	-21	Bubble appears at -5	V_i	0	$5.7\ 10^{-9}$	>100	270
		T_f	-5		V_f	$4.5\ 10^{-10}$	$1.5\ 10^{-8}$		
8	**Warming**	T_i	-21	Bubble appears at -5	V_i	0	$1.5\ 10^{-10}$	>100	380
		T_f	-5		V_f	$7.1\ 10^{-11}$	$5.7\ 10^{-10}$		
9	**Cooling**	T_i	-5	Bubble collapses at -11	V_i	$2.2\ 10^{-10}$	$3.6\ 10^{-9}$	-100	-60
		T_f	-12		V_f	0	$1.4\ 10^{-9}$		

Table 1

Figures:

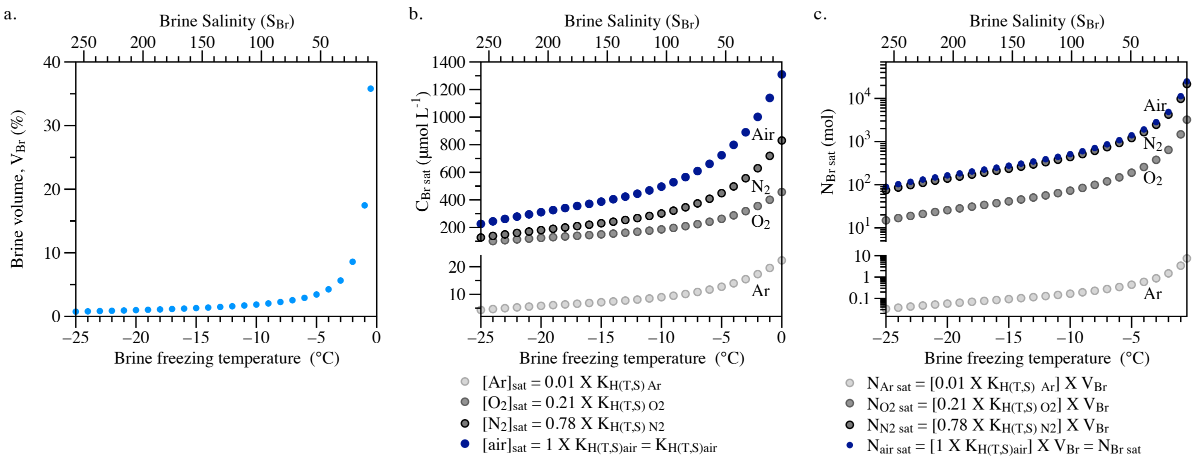
a.
Brine Salinity (S_Br)
250 200 150 100 50
Brine volume, V_Br (%)
0 10 20 30 40
−25 −20 −15 −10 −5 0
Brine freezing temperature (°C)
b.
Brine Salinity (S_Br)
C_Br sat (µmol L⁻¹)
1400 1200 1000 800 600 400 200
20 10
Air
N2
O2
Ar
Brine freezing temperature (°C)
[Ar]sat = 0.01 X KH(T,S) Ar
[O2]sat = 0.21 X KH(T,S) O2
[N2]sat = 0.78 X KH(T,S) N2
[air]sat = 1 X KH(T,S)air = KH(T,S)air
c.
Brine Salinity (S_Br)
N_Br sat (mol)
10⁴ 10³ 10² 10¹
10 1 0.1
Air
N2
O2
Ar
Brine freezing temperature (°C)
NAr sat = [0.01 X KH(T,S) Ar] X VBr
NO2 sat = [0.21 X KH(T,S) O2] X VBr
NN2 sat = [0.78 X KH(T,S) N2] X VBr
Nair sat = [1 X KH(T,S)air] X VBr = NBr sat

Figure 1

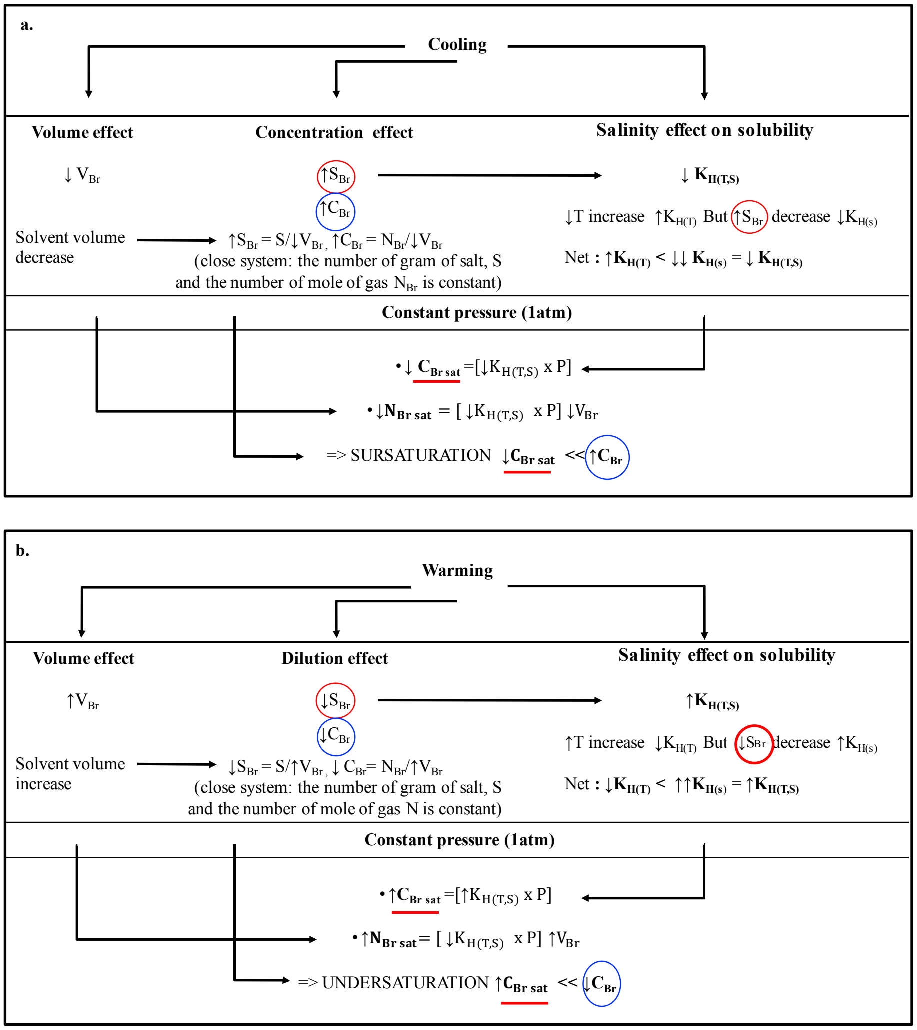
a.
Cooling
Volume effect
Concentration effect
Salinity effect on solubility
$\downarrow V_{Br}$
$\uparrow S_{Br}$
$\uparrow C_{Br}$
$\downarrow K_{H(T,S)}$
Solvent volume decrease
$\uparrow S_{Br} = S/\downarrow V_{Br}$, $\uparrow C_{Br} = N_{Br}/\downarrow V_{Br}$
(close system: the number of gram of salt, S and the number of mole of gas N_{Br} is constant)
$\downarrow$T increase $\uparrow K_{H(T)}$ But $\uparrow S_{Br}$ decrease $\downarrow K_{H(s)}$
Net : $\uparrow K_{H(T)} < \downarrow\downarrow K_{H(s)} = \downarrow K_{H(T,S)}$
Constant pressure (1atm)
• $\downarrow C_{Br\,sat} = [\downarrow K_{H(T,S)} \times P]$
• $\downarrow N_{Br\,sat} = [\downarrow K_{H(T,S)} \times P] \downarrow V_{Br}$
=> SURSATURATION $\downarrow C_{Br\,sat} << \uparrow C_{Br}$
b.
Warming
Volume effect
Dilution effect
Salinity effect on solubility
$\uparrow V_{Br}$
$\downarrow S_{Br}$
$\downarrow C_{Br}$
$\uparrow K_{H(T,S)}$
Solvent volume increase
$\downarrow S_{Br} = S/\uparrow V_{Br}$, $\downarrow C_{Br} = N_{Br}/\uparrow V_{Br}$
(close system: the number of gram of salt, S and the number of mole of gas N is constant)
$\uparrow$T increase $\downarrow K_{H(T)}$ But $\downarrow S_{Br}$ decrease $\uparrow K_{H(s)}$
Net : $\downarrow K_{H(T)} < \uparrow\uparrow K_{H(s)} = \uparrow K_{H(T,S)}$
Constant pressure (1atm)
• $\uparrow C_{Br\,sat} = [\uparrow K_{H(T,S)} \times P]$
• $\uparrow N_{Br\,sat} = [\downarrow K_{H(T,S)} \times P] \uparrow V_{Br}$
=> UNDERSATURATION $\uparrow C_{Br\,sat} << \downarrow C_{Br}$

Figure 2

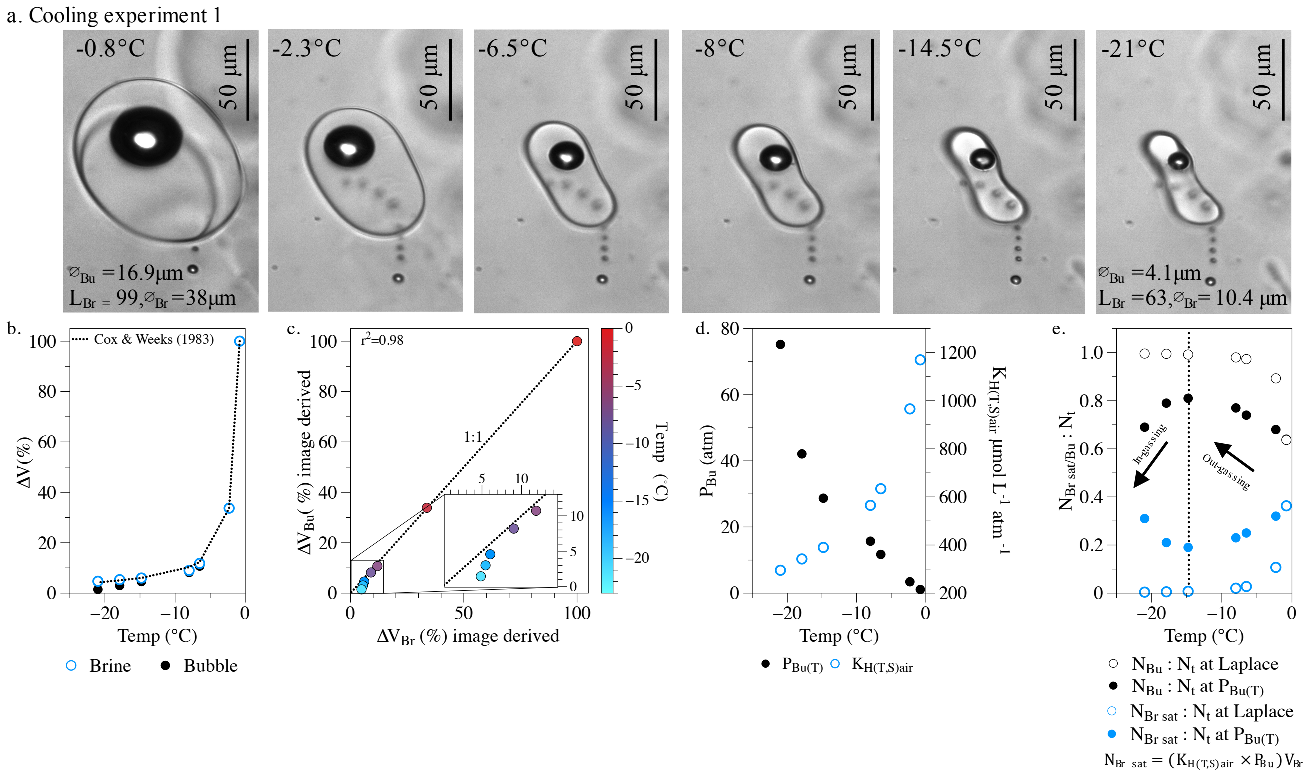
a. Cooling experiment 1
-0.8°C
-2.3°C
-6.5°C
-8°C
-14.5°C
-21°C
50 µm
⌀Bu =16.9µm
LBr = 99,⌀Br =38µm
⌀Bu =4.1µm
LBr =63,⌀Br= 10.4 µm
b.
Cox & Weeks (1983)
ΔV(%)
Temp (°C)
Brine
Bubble
c.
r²=0.98
1:1
ΔVBu(%) image derived
ΔVBr (%) image derived
Temp (°C)
d.
PBu (atm)
KH(T,S)air µmol L⁻¹ atm⁻¹
Temp (°C)
PBu(T)
KH(T,S)air
e.
In-gassing
Out-gassing
NBr sat/Bu : Nt
Temp (°C)
NBu : Nt at Laplace
NBu : Nt at PBu(T)
NBr sat : Nt at Laplace
NBr sat : Nt at PBu(T)
NBr sat = (KH(T,S)air × PBu) VBr

Figure 3

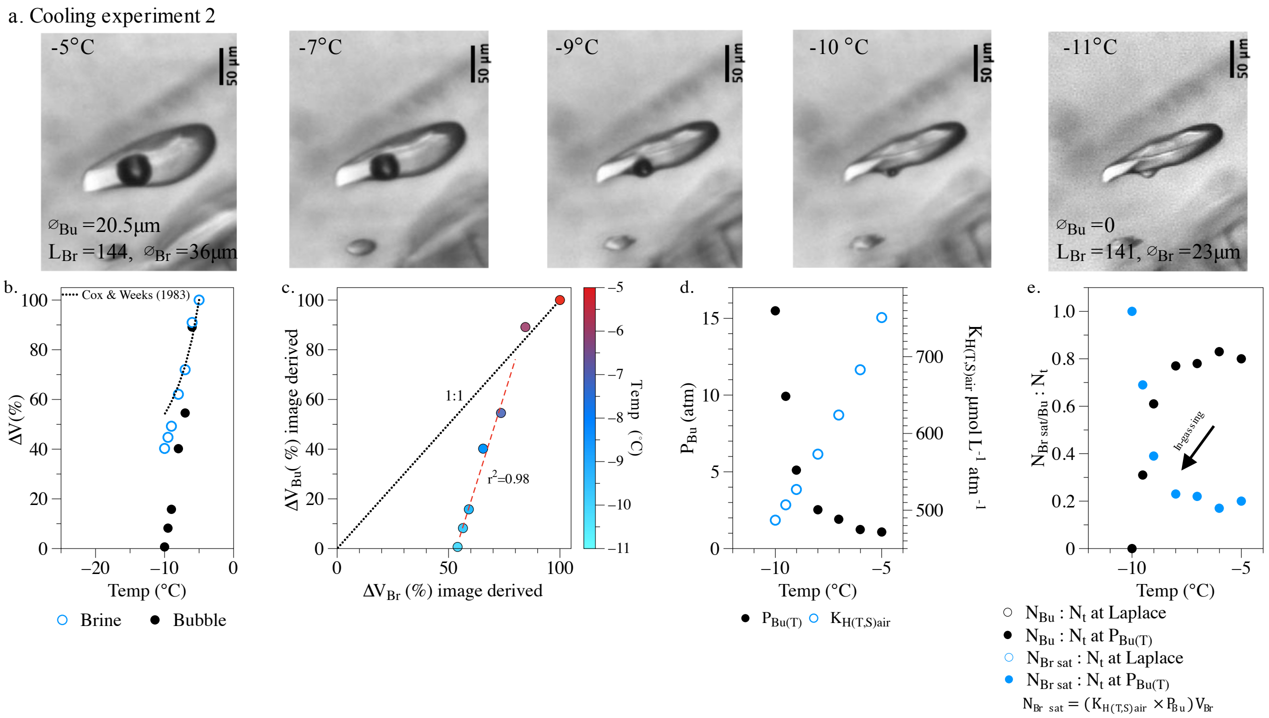
a. Cooling experiment 2
-5°C
50 µm
∅Bu =20.5µm
LBr =144, ∅Br =36µm
-7°C
-9°C
-10 °C
-11°C
∅Bu =0
LBr =141, ∅Br =23µm
b.
Cox & Weeks (1983)
ΔV(%)
Temp (°C)
Brine
Bubble
c.
ΔVBu(%) image derived
ΔVBr (%) image derived
1:1
r2=0.98
Temp (°C)
d.
PBu (atm)
KH(T,S)air µmol L-1 atm-1
Temp (°C)
PBu(T)
KH(T,S)air
e.
NBr sat/Bu : Nt
In-gassing
Temp (°C)
NBu : Nt at Laplace
NBu : Nt at PBu(T)
NBr sat : Nt at Laplace
NBr sat : Nt at PBu(T)
NBr sat = (KH(T,S)air × PBu)VBr

Figure 4

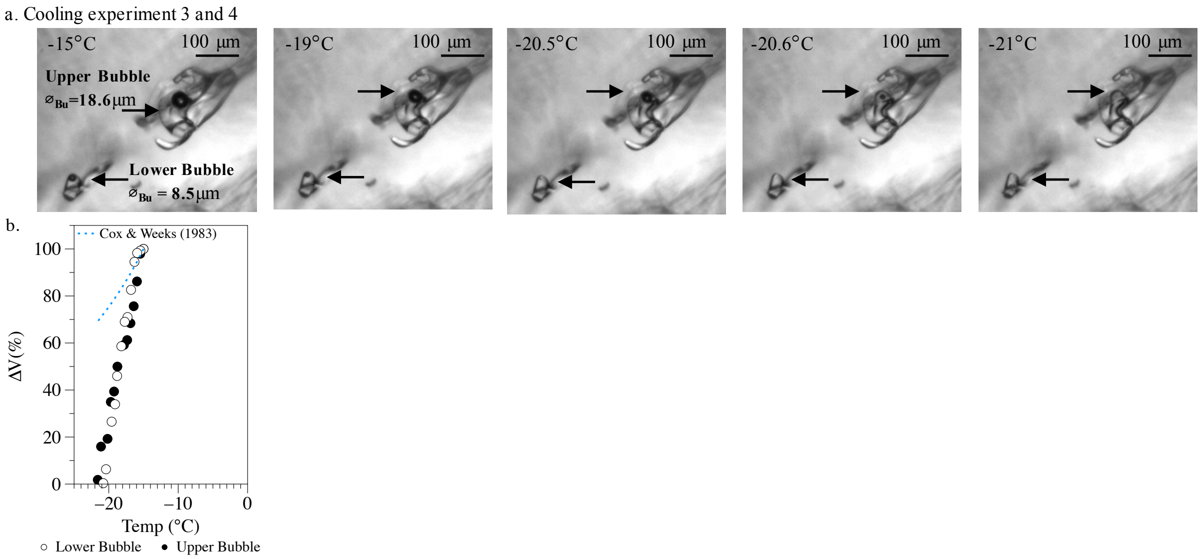
a. Cooling experiment 3 and 4
-15°C
100 μm
Upper Bubble
⌀Bu=18.6μm
Lower Bubble
⌀Bu = 8.5μm
-19°C
100 μm
-20.5°C
100 μm
-20.6°C
100 μm
-21°C
100 μm
b.
Cox & Weeks (1983)
ΔV(%)
100
80
60
40
20
0
−20
−10
0
Temp (°C)
○ Lower Bubble
● Upper Bubble

Figure 5

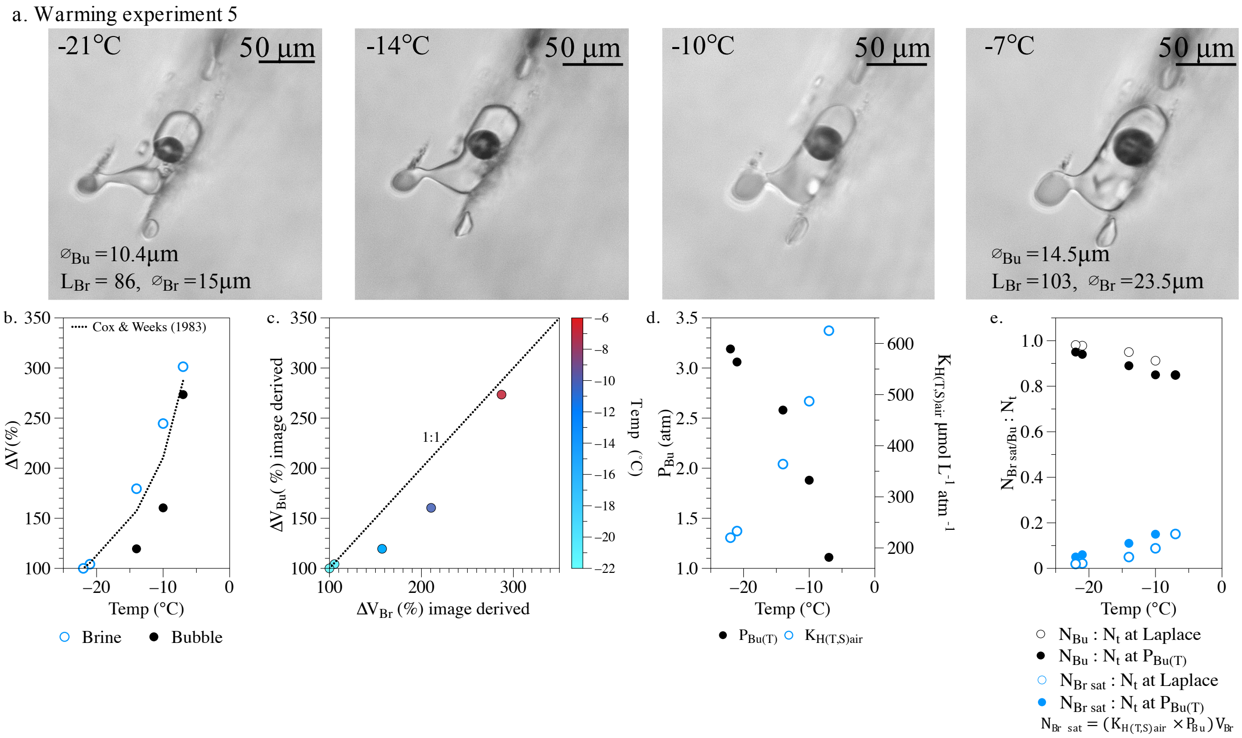
a. Warming experiment 5
-21°C
50 µm
⌀Bu =10.4µm
LBr = 86, ⌀Br =15µm
-14°C
50 µm
-10°C
50 µm
-7°C
50 µm
⌀Bu =14.5µm
LBr =103, ⌀Br =23.5µm
b.
Cox & Weeks (1983)
ΔV(%)
100
150
200
250
300
350
−20
−10
0
Temp (°C)
Brine
Bubble
c.
ΔVBu (%) image derived
ΔVBr (%) image derived
1:1
100
200
300
Temp (°C)
−6
−8
−10
−12
−14
−16
−18
−20
−22
d.
PBu (atm)
1.0
1.5
2.0
2.5
3.0
3.5
KH(T,S)air µmol L-1 atm-1
200
300
400
500
600
Temp (°C)
PBu(T)
KH(T,S)air
e.
NBr sat/Bu : Nt
0
0.2
0.4
0.6
0.8
1.0
Temp (°C)
NBu : Nt at Laplace
NBu : Nt at PBu(T)
NBr sat : Nt at Laplace
NBr sat : Nt at PBu(T)
NBr sat = (KH(T,S)air × PBu)VBr

Figure 6

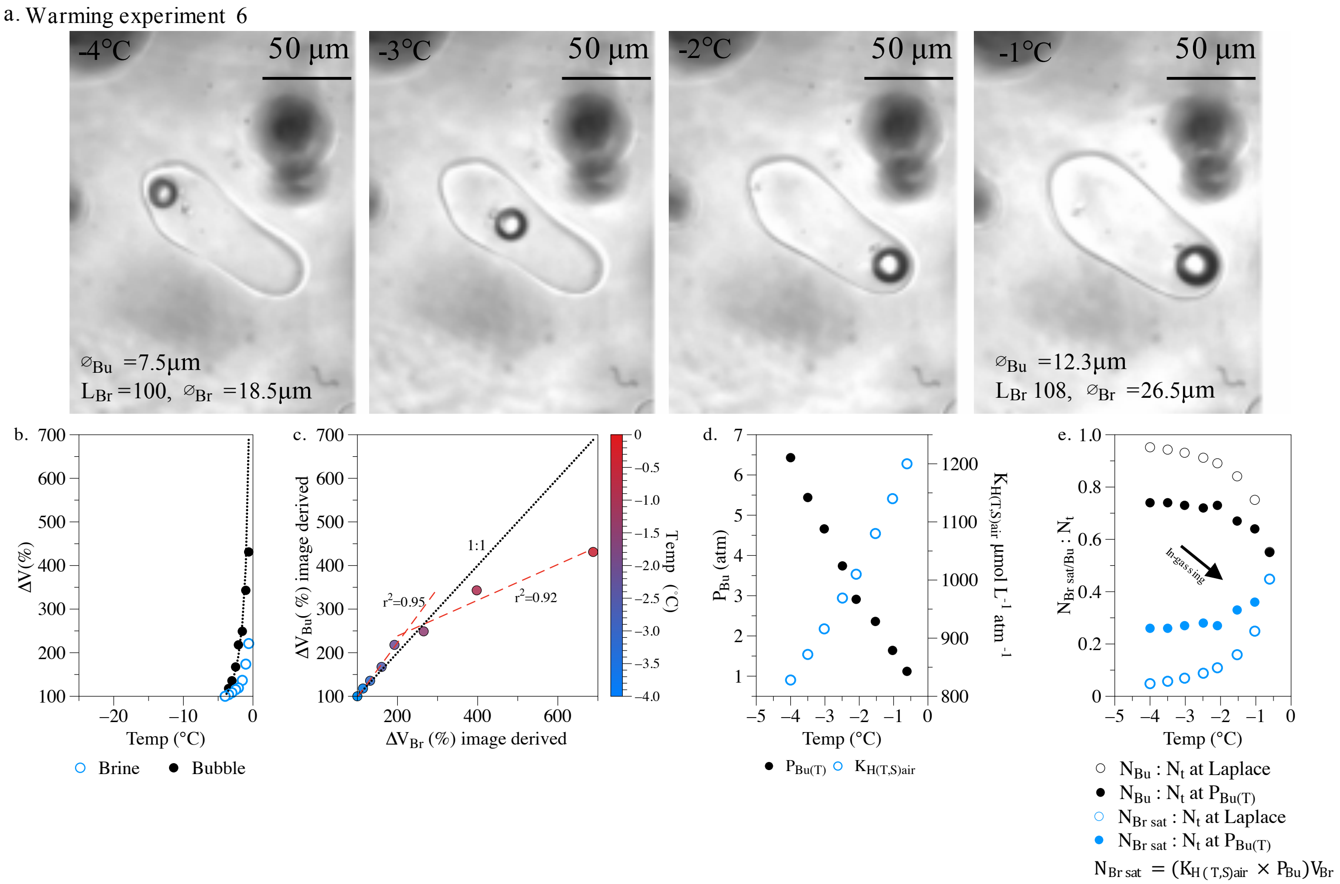
a. Warming experiment 6
-4°C
50 µm
-3°C
50 µm
-2°C
50 µm
-1°C
50 µm
⌀Bu =7.5µm
LBr =100, ⌀Br =18.5µm
⌀Bu =12.3µm
LBr 108, ⌀Br =26.5µm
b.
ΔV(%)
700
600
500
400
300
200
100
−20
−10
0
Temp (°C)
○ Brine
● Bubble
c.
ΔVBu (%) image derived
ΔVBr (%) image derived
700
600
500
400
300
200
100
200
400
600
1:1
r2=0.95
r2=0.92
Temp (°C)
0
−0.5
−1.0
−1.5
−2.0
−2.5
−3.0
−3.5
−4.0
d.
PBu (atm)
7
6
5
4
3
2
1
KH(T,S)air µmol L-1 atm -1
1200
1100
1000
900
800
−5
−4
−3
−2
−1
0
Temp (°C)
● PBu(T)
○ KH(T,S)air
e.
NBr sat/Bu : Nt
1.0
0.8
0.6
0.4
0.2
0
−5
−4
−3
−2
−1
0
Temp (°C)
In-gassing
○ NBu : Nt at Laplace
● NBu : Nt at PBu(T)
○ NBr sat : Nt at Laplace
● NBr sat : Nt at PBu(T)
NBr sat = (KH (T,S)air × PBu)VBr

Figure 7

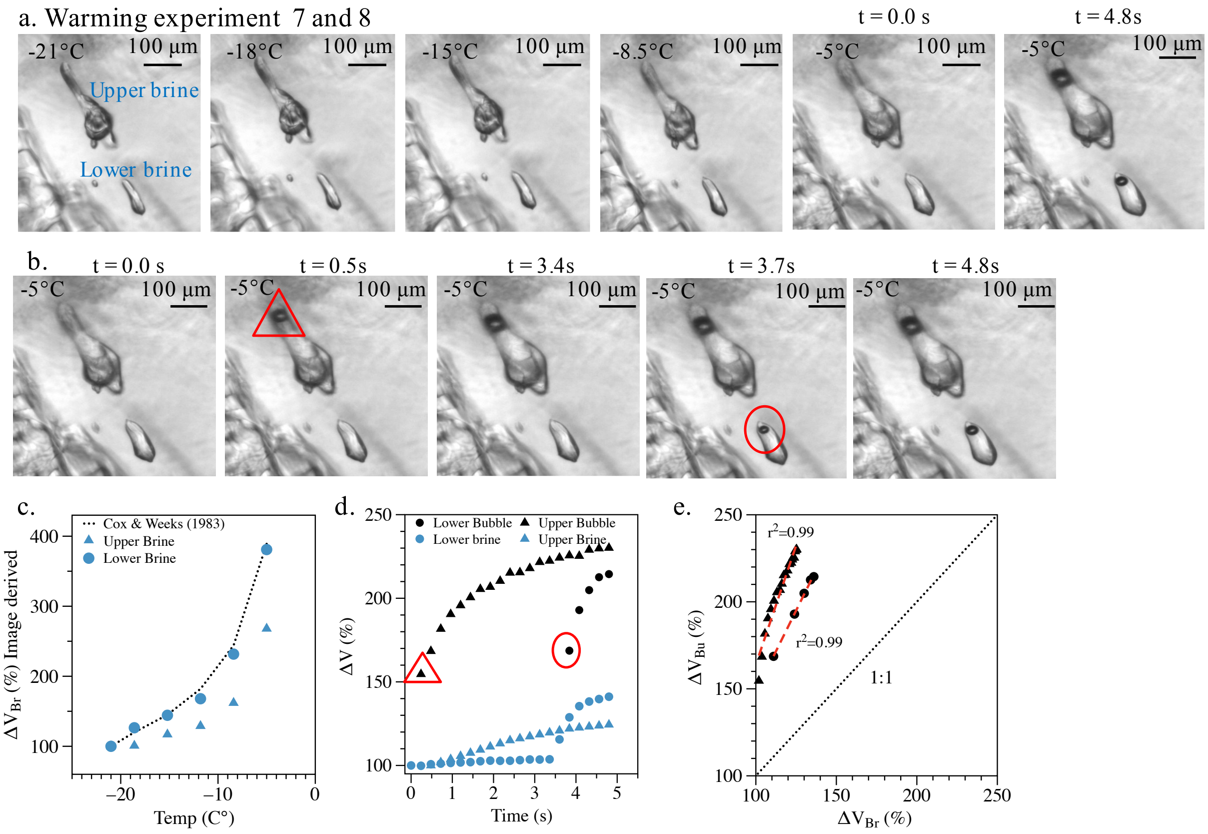
a. Warming experiment 7 and 8
-21°C
-18°C
-15°C
-8.5°C
t = 0.0 s
-5°C
t = 4.8s
-5°C
100 μm
Upper brine
Lower brine
b.
t = 0.0 s
t = 0.5s
t = 3.4s
t = 3.7s
t = 4.8s
-5°C
100 μm
c.
Cox & Weeks (1983)
Upper Brine
Lower Brine
ΔV_Br (%) Image derived
Temp (C°)
400
300
200
100
−20
−10
0
d.
Lower Bubble
Upper Bubble
Lower brine
Upper Brine
ΔV (%)
Time (s)
250
200
150
100
0
1
2
3
4
5
e.
r²=0.99
r²=0.99
1:1
ΔV_Bu (%)
ΔV_Br (%)
250
200
150
100
100
150
200
250

Figure 8

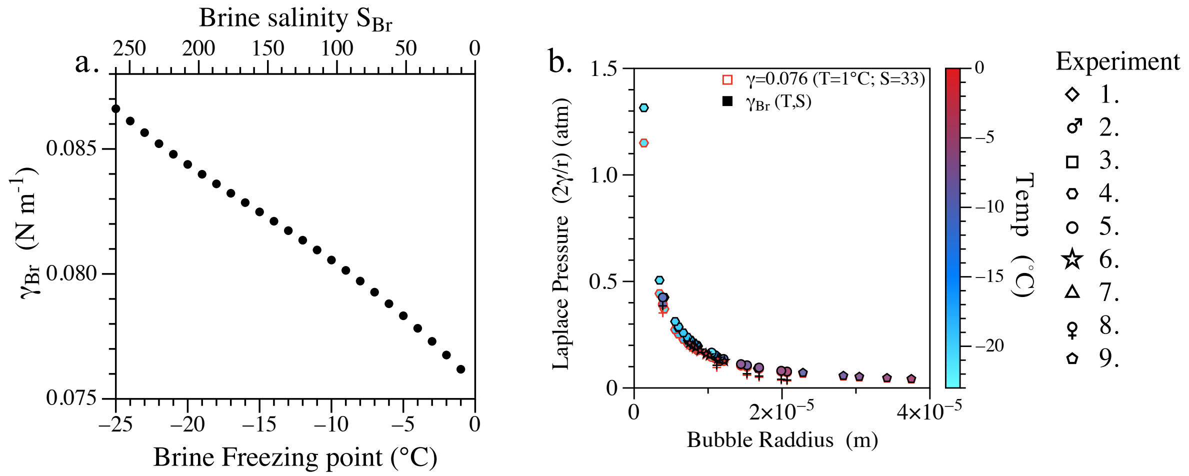
a.
Brine salinity S_{Br}
250
200
150
100
50
0
γ_{Br} (N m^{-1})
0.085
0.080
0.075
−25
−20
−15
−10
−5
0
Brine Freezing point (°C)
b.
Laplace Pressure (2γ/r) (atm)
1.5
1.0
0.5
0
□ γ=0.076 (T=1°C; S=33)
■ γ_{Br} (T,S)
0
2×10^{-5}
4×10^{-5}
Bubble Raddius (m)
Temp (°C)
0
−5
−10
−15
−20
Experiment
◇ 1.
♂ 2.
□ 3.
⬡ 4.
○ 5.
☆ 6.
△ 7.
♀ 8.
⬠ 9.

Figure 9

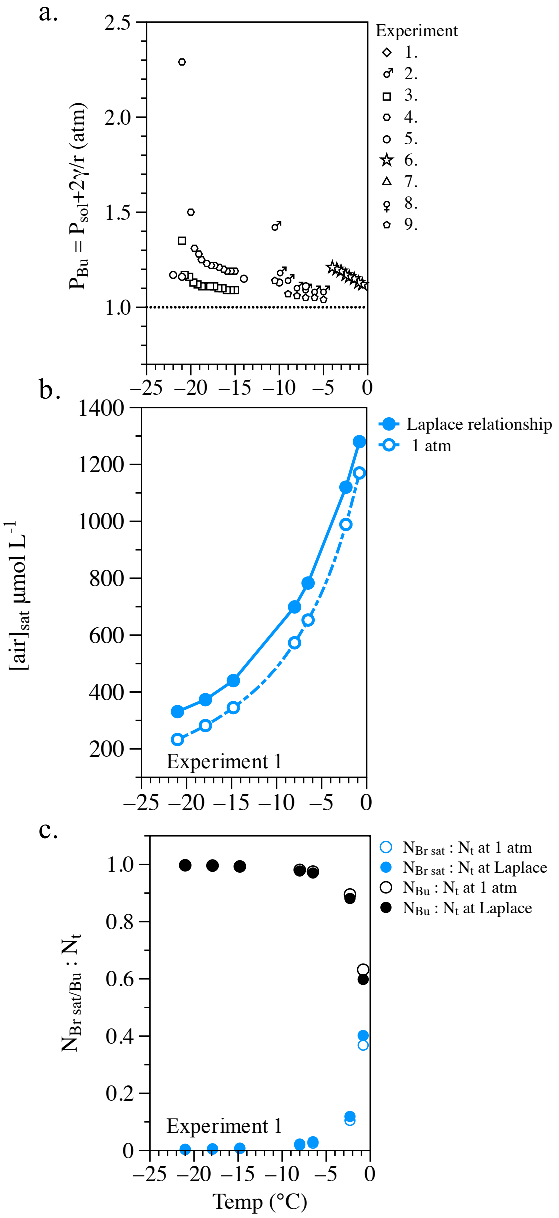
a.
$P_{Bu} = P_{sol}+2\gamma/r$ (atm)
2.5
2.0
1.5
1.0
−25 −20 −15 −10 −5 0
Experiment
◇ 1.
♂ 2.
□ 3.
○ 4.
○ 5.
☆ 6.
△ 7.
♀ 8.
⬠ 9.
b.
$[air]_{sat}$ µmol L^{-1}
1400
1200
1000
800
600
400
200
Experiment 1
−25 −20 −15 −10 −5 0
● Laplace relationship
○ 1 atm
c.
$N_{Br\ sat/Bu} : N_t$
1.0
0.8
0.6
0.4
0.2
0
Experiment 1
−25 −20 −15 −10 −5 0
Temp (°C)
○ $N_{Br\ sat} : N_t$ at 1 atm
● $N_{Br\ sat} : N_t$ at Laplace
○ $N_{Bu} : N_t$ at 1 atm
● $N_{Bu} : N_t$ at Laplace

Figure 10

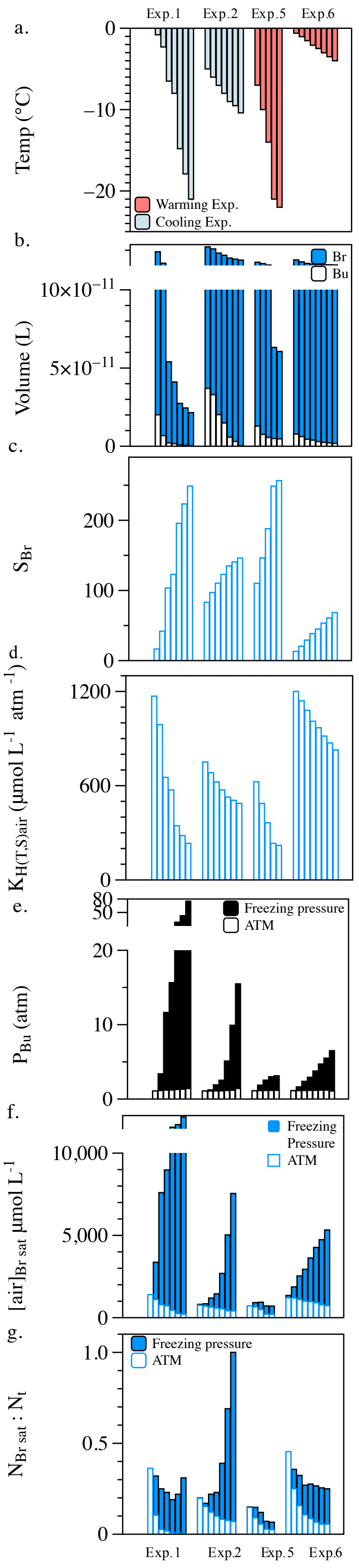
Exp.1
Exp.2
Exp.5
Exp.6
a.
Temp (°C)
0
−10
−20
Warming Exp.
Cooling Exp.
b.
Volume (L)
10×10⁻¹¹
5×10⁻¹¹
0
Br
Bu
c.
S_Br
200
100
0
d.
K_H(T,S)air (μmol L⁻¹ atm⁻¹)
1200
600
0
e.
P_Bu (atm)
80
50
20
10
0
Freezing pressure
ATM
f.
[air]_Br sat μmol L⁻¹
10,000
5,000
0
Freezing Pressure
ATM
g.
N_Br sat : N_t
1.0
0.5
0
Freezing pressure
ATM
Exp.1
Exp.2
Exp.5
Exp.6

Figure 11

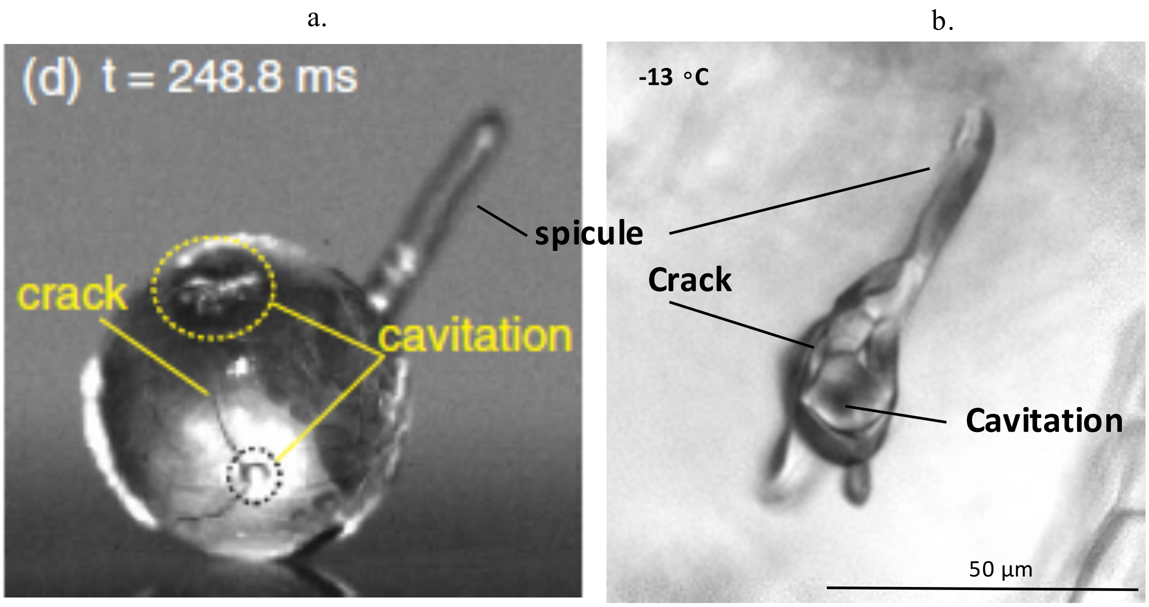
a.
(d) t = 248.8 ms
crack
cavitation
spicule
b.
-13 °C
Crack
Cavitation
50 µm

Figure 12